International Journal of Multiphase Flow 174 (2024) 104764

Contents lists available at ScienceDirect

International Journal of Multiphase Flow

journal homepage: www.elsevier.com/locate/ijmulflow

Clustering, rotation, and swirl of inertial particles in turbulent channel flow

Jacob R. West [a,*], Thibault Maurel–Oujia [b,*], Keigo Matsuda [c], Kai Schneider [b], Suhas S. Jain [d,e], Kazuki Maeda [f]

[a] Department of Mechanical Engineering, Stanford University, Stanford, CA, USA
[b] Institut de Mathématiques de Marseille, Aix-Marseille Université, CNRS, Marseille, France
[c] Japan Agency for Marine-Earth Science and Technology (JAMSTEC), Yokohama, Japan
[d] George W. Woodruff School of Mechanical Engineering, Georgia Institute of Technology, Atlanta, GA, USA
[e] Center for Turbulence Research, Stanford University, Stanford, CA, USA
[f] School of Aeronautics and Astronautics, Purdue University, West Lafayette, IN, USA

ARTICLE INFO

Keywords:
Turbulent channel flow
Inertial particles
Clustering dynamics
Tessellation-based analysis
Stokes number
Mass loading

ABSTRACT

Clustering dynamics of inertial particles in turbulent channel flow are studied via tessellation-based analysis of high-fidelity simulation data at $Re_\tau \approx 230$ with various values of mass loading (10% – 100%) and the Stokes number ($St^+ = [1 - 60]$). We then characterise the solenoidal, rotational, and swirling motions of clusters by computing the probability density functions (PDFs) of the divergence, curl, and helicity of the particle velocity, as well as their dependence on wall-normal distance, using the methods of Oujia et al. (2020); Maurel–Oujia et al. (2023). Particle inertia gives heavier tails to the PDFs of divergence and curl, suggesting enhanced intermittency in the convergence/divergence of clusters, and in their rotational motions. The fluctuations of the divergence and curl are most intense in the buffer layer, due to the stronger fluctuations of fluid velocity there. Similarities are identified between the cluster dynamics in the logarithmic region and those in homogeneous isotropic turbulence, including the dependence of divergence, curl, and helicity on Stokes number. The effect of increasing mass loading on cluster dynamics is relatively small except in the viscous sublayer, where attenuation of clustering, rotation, and swirling motions are observed. The effect of increasing Stokes number on the viscous sublayer is different, resulting in more intense convergence/divergence and rotation of particle clusters, as the particles become more independent of the carrier fluid.

1. Introduction

Particle-laden turbulent flows over walls occur in many natural and engineering systems. Examples include sediment transport in rivers, dust storms in the atmospheric boundary layer (Hutter, 2005), chemical processes in industrial riser reactors (Basu, 2006), and novel radiation absorbers in concentrating solar power plants (Ho, 2016). In all of these systems, particles form clusters and voids due to interaction with the turbulence. Clustering also affects the optical depth in gas flows laden with particles, which is particularly important in the design of particle-based solar receivers (Frankel et al., 2017) and in radiation absorption in clouds (Matsuda et al., 2012). The complex physics of cluster formation, combined with the strong turbulence modulation which occurs at high mass loading, makes these flows difficult to predict and model (Balachandar and Eaton, 2010). In addition, the large optical depth makes them difficult to study experimentally, making simulations an essential tool to improve understanding.

Particle clustering is known to be weak at very small and very large Stokes numbers and to peak at intermediate Stokes numbers. In the limit of small Stokes number, this can be explained by particles preferentially concentrating in regions of low vorticity and high strain Maxey (1987), Squires and Eaton (1991), i.e. they are centrifuged out of eddies because of their finite inertia. For moderate to large Stokes number, the explanation of decreased clustering is an area of ongoing interest. The ability of higher Stokes number particles to be affected by the history of their trajectories appears to be an important factor (Bragg and Collins, 2014; Liu et al., 2020). Other researchers point to the sweep-stick mechanism, which suggests that particles stick to zero-acceleration points in the flow, which are swept along by large-scale eddies (Chen et al., 2006; Coleman and Vassilicos, 2009). Recent work by Esmaily-Moghadam and Mani (2016) and Esmaily and Mani (2020) has succeeded in predicting the non-monotonic trend in clustering by analysing the Lyapunov exponents of small-scale particle clouds. At small Stokes number, this depends on local flow characteristics, but as Stokes number increases, the flow history and structure become increasingly dominant.

* Corresponding authors.
E-mail addresses: jrwest@alumni.stanford.edu (J.R. West), thibault.oujia@univ-amu.fr (T. Maurel–Oujia).

https://doi.org/10.1016/j.ijmultiphaseflow.2024.104764
Received 14 September 2023; Received in revised form 28 January 2024; Accepted 11 February 2024
Available online 13 February 2024

In channel flow, the dynamics of particle clustering are affected by the presence of the wall. It is known that particles tend to accumulate in regions of low turbulence intensity, such as near the wall, a phenomenon known as turbophoresis (Reeks, 1983). This tends to increase the particle concentration, but inter-particle collisions counteract this and play an important role in determining the equilibrium concentration near the wall (Li et al., 2001; Vreman, 2007). Furthermore, many experimental and computational studies have found that particles in the viscous sublayer and buffer layers accumulate in elongated streaks (Marchioli and Soldati, 2002; Soldati and Marchioli, 2009; Sardina et al., 2012; Fong et al., 2019). These correspond to the low-speed streaks in the fluid velocity (Robinson, 1991). Sweeps and ejections in wall turbulence also play an important role in cluster dynamics and near-wall accumulation (Marchioli and Soldati, 2002). As a result, clusters are constantly formed and annihilated as well as subjected to strong rotational motions near the wall. Fessler et al. (1994) studied particle clustering in the channel centreline using experiments with heavy particles. They found a peak in preferential concentration at intermediate Stokes numbers, and a systematic shift of clustering to smaller scales as the Stokes number decreases. Nilsen et al. (2013) used Voronoi tessellation to study particle clustering in a one-way coupled channel flow at different wall-normal distances. They found that preferential concentration (measured by the variance of the Voronoi volume PDF) peaked at an intermediate Stokes number and was strongest close to the wall and around the channel centre. They and Capecelatro and Desjardins (2015) also studied the effect of gravity on clustering in channel flow, both finding that in flows aligned with gravity, particles migrate towards the channel centre, but migrate towards the wall in flows against gravity. Nilsen et al. (2013) attribute this to the particles' mean velocity dictating which eddies they preferentially sample. At large mass loading with significant two-way coupling, Capecelatro and Desjardins (2015) hypothesise that the accumulation is due to minimisation of local drag. Fong et al. (2019) found in their channel flow experiments significant differences in particle clustering depending on wall-normal location. Clusters showed a preference for streamwise alignment throughout the flow, but this became more pronounced closer to the wall.

In addition to clustering, an important feature of particle-laden flows is that the particles exert drag forces back on the flow, and many authors have studied the effect of two-way coupled particles on wall-bounded flows. We present highlights of the literature relevant to this work, but refer readers to reviews by Balachandar and Eaton (2010) and Brandt and Coletti (2022) for greater depth. Experiments by Kulick et al. (1994) showed that at a mass loading of 0.1, the particle phase noticeably attenuates the fluid velocity fluctuations in turbulent channel flow, and this attenuation increases with mass loading. Turbulence attenuation with an increase in mass loading was also confirmed in an early computational study of particle laden channel flow by Li et al. (2001). They also found that the anisotropy of fluid Reynolds stresses greatly increased with mass loading. Vreman (2007) studied particle-laden vertical pipe flow over a mass loading range of 0.11 to 30 and also found that turbulence is significantly suppressed with larger mass loading. Lee and Lee (2015) explored the effect of Stokes number at mass loading of 0.3 using point-particle simulations, finding that particles with very low inertia could enhance the fluid turbulence, while larger particles attenuate it, and that maximum preferential concentration of particles occurred at a moderate Stokes number. In the context of turbulent Couette flow, Richter and Sullivan (2013) found that with an increase in mass loading the viscous stresses remain nearly constant while the fluid turbulent stress becomes weaker, and is replaced by a stress due to fluctuations in particle velocity. Recently, Costa et al. (2021) studied near-wall turbulence modulation with small particles up to mass loadings of 0.5, with the goal of reconciling conflicting reports about two-way coupled channel flows, such as observations of drag increase and decrease. They used particle-resolved simulations and found many of the same features as earlier studies regarding the effect of mass loading, including decreased turbulence intensity, increased anisotropy, and a transfer of Reynolds stresses from the fluid to particle phase.

In the present work, we study the clustering, rotation, and swirl of particle clouds in a turbulent channel flow with dilute volume fraction, but with mass loading $\mathcal{O}(1)$, which makes making the effect of the particles on the carrier phase dynamics significant. These flows are impractical to simulate with particle-resolved direct numerical simulations, so we opt for an Euler–Lagrange approach (Kuerten, 2016), which allows for exploration of a wide range of mass loading and Stokes numbers at affordable cost. The large number of particles also makes analysis of particle clustering difficult, motivating the use of new methods for doing so.

A useful numerical tool for analysing particle clustering in Euler–Lagrange simulations is tessellation. In brief, a tessellation decomposes a domain into geometric shapes. This is useful for analysing particle clustering by defining a tessellation based on the particle locations. Monchaux et al. (2010) used the Voronoi tessellation to characterise the effect of Stokes number on particle clustering. This technique has been widely applied in homogeneous isotropic turbulence, and to a lesser extent in wall-bounded flows (e.g. Nilsen et al., 2013). To gain further insight into the dynamics of particle clouds, tessellation-based techniques have been developed recently to compute velocity gradients from dispersed particle data. Oujia et al. (2020) proposed a method to quantify the formation of clusters and voids by computing the time change of the tessellation cell volume. A method for computing the curl of the particle velocity was also introduced in Oujia et al. (2022), Maurel-Oujia et al. (2023), in order to quantify the rotation of particle clouds.

Knowing the curl, the helicity of the particle motion can also be determined, which yields insight into the processes that determine the flow topology (Moffatt and Tsinober, 1992). Swirling flows are characterised by strong helicity, and in the turbulence community, helicity has been used to characterise three-dimensional swirling coherent structures, which correspond to flow regions of maximum helicity (Farge et al., 2001). Similarly, the helicity of the particle velocity can be used to determine whether particle motions are two-dimensional (zero helicity) or three-dimensional.

The goal of the present work is to bring detailed insights into the clustering and motion of heavy, inertial particles in wall turbulence, in the regime of moderate mass loading. This is accomplished by applying tessellation-based analysis to a set of numerical data of high-fidelity, four-way coupled Euler–Lagrange simulations. Unlike in homogeneous isotropic turbulence (HIT), the cluster dynamics in channel flow have a strong dependence on their wall-normal distance. In order to quantify this dependence, we compute the probability density functions (PDFs) of divergence, curl, and helicity in the viscous sublayer, buffer layer, and logarithmic layers for both fluid and particle phases. To the best of our knowledge, such an analysis has not been previously performed.

The effects of particle mass loading and Stokes number on the PDFs of each layer are characterised with the aid of flow visualisations obtained by colouring particles with divergence, vorticity magnitude, or helicity. In the log layer, in which small-scale turbulence becomes more homogeneous and isotropic than the other layers, differences and similarities with the previous results of HIT are discussed with comparisons to the work of Matsuda et al. (2014) and Oujia et al. (2020), especially with respect to the dependence of clustering on Stokes number. Matsuda et al. (2014) found that as Stokes number was increased, the energy spectra of particle number density increased in intensity while retaining the same shape before shifting to a peak at larger scales above a critical Stokes number. Oujia et al. (2020) found a saturation at a critical Stokes number in the intensity of divergence/convergence values. Similar saturation is observed qualitatively in the log layer results presented here. Finally, the particle-based Fourier transform is used to obtain scale information on the particle number density distribution, and to understand what scales of clustering contribute to

the trends observed in the PDFs. Preliminary versions of this study were reported in West et al. (2022) and West (2023).

The remainder of this manuscript is organised as follows. In Section 2, the numerical methods used in this work are described, including the channel flow simulation database (Section 2.1), the tessellation approach for obtaining divergence, curl, and helicity (Section 2.2), and the method for calculating Fourier spectra of particle number density fluctuations (Section 2.3). Section 3 presents Eulerian statistics for the fluid phase (Section 3.1) and Lagrangian statistics for the particle phase, considering the effect of Stokes number (Section 3.2.1) and mass loading (Section 3.2.2). Fourier spectra of number density fluctuations are likewise analysed (Section 3.3). Finally, conclusions are drawn in Section 4.

2. Methods

2.1. Channel flow simulations

The four-way coupled particle-laden channel flow simulations were performed using the Soleil-MPI code, which is briefly described here; more details can be found in Esmaily et al. (2020). The Navier–Stokes equations for incompressible flow with particle two-way coupling terms are solved as

$$\frac{\partial(\rho \boldsymbol{u})}{\partial t} + \nabla \cdot (\rho \boldsymbol{u} \otimes \boldsymbol{u}) = -\nabla p + \mu \nabla^2 \boldsymbol{u} + \sum_{m=1}^{N_p} \boldsymbol{f}^{(m)} \delta_{\text{Dirac}}(\boldsymbol{x} - \boldsymbol{x}_p{}^{(m)}), \tag{1}$$

where $\boldsymbol{u}$ is the fluid velocity, ρ is the (constant) fluid density, p is the hydrodynamic pressure and μ is the dynamic viscosity. The last term is the summation of the two-way coupling force contribution from each particle $\boldsymbol{f}^{(m)}$, over all particles N_p, based on the Dirac-delta function $\delta_{\text{Dirac}}(\cdot)$, which has units of inverse volume, and whose argument is the distance between a position in the fluid $\boldsymbol{x}$ and a given particle $\boldsymbol{x}_p{}^{(m)}$. Because all simulation cases in this work have a small particle volume fraction (less than 1.5×10^{-4}), the volume displacement effect has been ignored. The particle drag force uses the drag correlation for finite Reynolds numbers from (Schiller and Naumann, 1935), which is given by

$$\boldsymbol{f}^{(m)} = 3\pi\mu D_p \left(1 + 0.15 Re_p^{0.687}\right)\left(\boldsymbol{v}_p^{(m)} - \widetilde{\boldsymbol{u}}^{(m)}\right), \tag{2}$$

where D_p is the particle diameter, $\boldsymbol{v}_p^{(m)}$ is the velocity of particle m, $\widetilde{\boldsymbol{u}}^{(m)}$ is the undisturbed fluid velocity at the particle location, and $Re_p = \rho D_p |\boldsymbol{v}_p^{(m)} - \widetilde{\boldsymbol{u}}^{(m)}|/\mu$ is the particle Reynolds number.

Soleil-MPI solves the above equations using a finite-volume method with second-order explicit spatial derivatives. At each timestep, a pressure Poisson equation is solved using a geometric multigrid method to achieve a divergence-free velocity field. The two-way-coupling terms in the momentum equations are obtained by distributing the force associated with each particle to the surrounding grid points using trilinear interpolation, using the correction scheme proposed by Esmaily and Horwitz (2018) to account for particle disturbances on the fluid velocity.

Each particle trajectory is computed according to the equations of motion for a single particle of mass m_p, neglecting gravity, as

$$\dot{\boldsymbol{x}}_p^{(m)} = \boldsymbol{v}_p^{(m)}, \tag{3}$$

$$m_p \dot{\boldsymbol{v}}_p^{(m)} = -\boldsymbol{f}^{(m)}. \tag{4}$$

Recent works have indicated that gravity can have a significant effect on particle distribution and dynamics, depending on the Stokes number and other flow parameters (Lee and Lee, 2019; Bragg et al., 2021), but we neglect this effect here for simplicity. Time advancement for both the Eulerian fluid variables and the Lagrangian point particles is done with a second-order Runge–Kutta method. Collisions with walls and other particles are accounted for assuming perfectly elastic collisions according to the hard sphere model.

Table 1
Parameters of the channel flow data: the friction Reynolds number Re_τ, the number of particles N_p, the particle to fluid density ratio ρ_p/ρ, the overall mass loading ϕ_0, the average mass loading in the viscous sublayer ϕ_{visc}, the average mass loading in the buffer layer ϕ_{buf}, the average mass loading in the logarithmic layer ϕ_{log}, the friction Stokes number St^+, and the Kolmogorov Stokes number based on the dissipation rate averaged over the logarithmic layer St_η^{log}.

	Re_τ	N_p	ρ_p/ρ	ϕ_0	ϕ_{visc}	ϕ_{buf}	ϕ_{log}	St^+	St_η^{log}
Flow 0	229	0	N/A	0	0	0	0	N/A	N/A
Flow 1	225	1.43×10^7	7.42×10^3	0.1	1.37	0.13	0.06	6.90	0.69
Flow 2	227	5.70×10^7	7.42×10^3	0.4	2.36	0.59	0.32	7.01	0.59
Flow 3	234	1.43×10^8	7.42×10^3	1.0	3.54	1.41	0.88	7.45	0.54
Flow 4	263	1.43×10^9	7.42×10^2	1.0	1.52	1.12	0.98	1.02	0.075
Flow 5	273	4.51×10^8	2.35×10^3	1.0	2.63	1.31	0.93	2.98	0.21
Flow 6	213	4.51×10^7	2.35×10^4	1.0	2.79	1.58	0.85	19.6	1.42
Flow 7	210	1.43×10^7	7.42×10^4	1.0	2.10	1.47	0.89	60.0	3.66

A suite of particle-laden channel flow cases, described in Table 1, are used in this work to assess the role of mass loading and Stokes number. Mass loading is defined as the ratio of particle mass to fluid mass: $\phi = nm_p/\rho$, where n is the particle number density. Each case is described by the mass loading averaged over the domain, ϕ_0, but ϕ varies in time and space for each flow due to preferential concentration and turbophoresis. Due to turbophoresis, the mass loading decreases with wall distance, as indicated by the average mass loadings for each flow region in Table 1. The Stokes number primarily used in this work is the friction Stokes number, $St^+ = \tau_p/\tau_{visc}$, which is the ratio of the particle relaxation time scale $\tau_p = \rho_p D_p^2/(18\mu)$ to the viscous time scale associated with the wall shear stress $\tau_{visc} = \delta/\sqrt{\tau_w/\rho}$. The channel half-height is δ, ρ_p is the particle density, and τ_w is the wall shear stress. Table 1 also includes the Kolmogorov Stokes number St_η^{log}, which is defined based on the dissipation rate ϵ of turbulent kinetic energy averaged over the range $50 < y^+ \leq Re_\tau$, i.e., $St_\eta^{\text{log}} = \tau_p\sqrt{\rho\epsilon/\mu}$. Here, y^+ is the wall-normal coordinate normalised by the viscous length scale $l_{visc} = \mu/\sqrt{\rho\tau_w}$. St_η^{log} is used to facilitate comparison with results from HIT. The cases in which St^+ is varied all have $\phi_0 = 1$, at which interphase coupling is strong, and the cases in which ϕ_0 is varied all have $St^+ \approx 7$, at which a strong degree of preferential concentration is expected based on the simulations of Lee and Lee (2015).

The fluid and particle properties are based on the benchmark experiments and computations described in Esmaily et al. (2020), with a channel geometry instead of a duct. These experiments used small nickel particles in a turbulent air flow. Accordingly, in our simulations, the carrier fluid is air, with $\rho = 1.2$ kg/m^3 and $\mu = 1.87 \times 10^{-5}$ Pa-s, and the particles are monodisperse spheres with diameter $D_p = 11.5$ μm. In terms of the Kolmogorov length scale in the logarithmic layer, the particles range from $D_p^\eta = [0.03 - 0.043]$, permitting the use of the point-particle approximation. The average mass loading ϕ_0 is varied by changing the number of particles, using a constant particle density of $\rho_p = 8900$ kg/m^3 (the density of nickel). The Stokes number St^+ is varied by changing the particle density and number of particles at a constant ϕ_0. Across all simulation cases, the fluid mass flux is held constant. As N_p and ρ_p are varied, Re_τ varies slightly from the no-particle value. This indicates either drag reduction (Re_τ decrease) or drag enhancement (Re_τ increase). Small amounts of drag reduction due to two-way coupling have been observed in some other studies, as described by Zhao et al. (2013), while more recent particle-resolved simulations have shown only drag increase for $\phi_0 < 0.5$ (Costa et al., 2021). The small changes in Re_τ contribute to small changes in St^+, as indicated in Table 1.

For all cases except Flow 4, the overall volume fraction, $\alpha_0 = \phi_0/((\rho_p/\rho_f) + \phi_0)$, is less than 10^{-3}, which is generally considered the threshold above which inter-particle collisions (i.e. four-way coupling) become important (Elghobashi, 1994). In the case of Flow 4, $\alpha_0 = 1.35 \times 10^{-3}$, so collisions are still expected to have marginal relevance to particle-turbulence interaction. However, collisions are still included

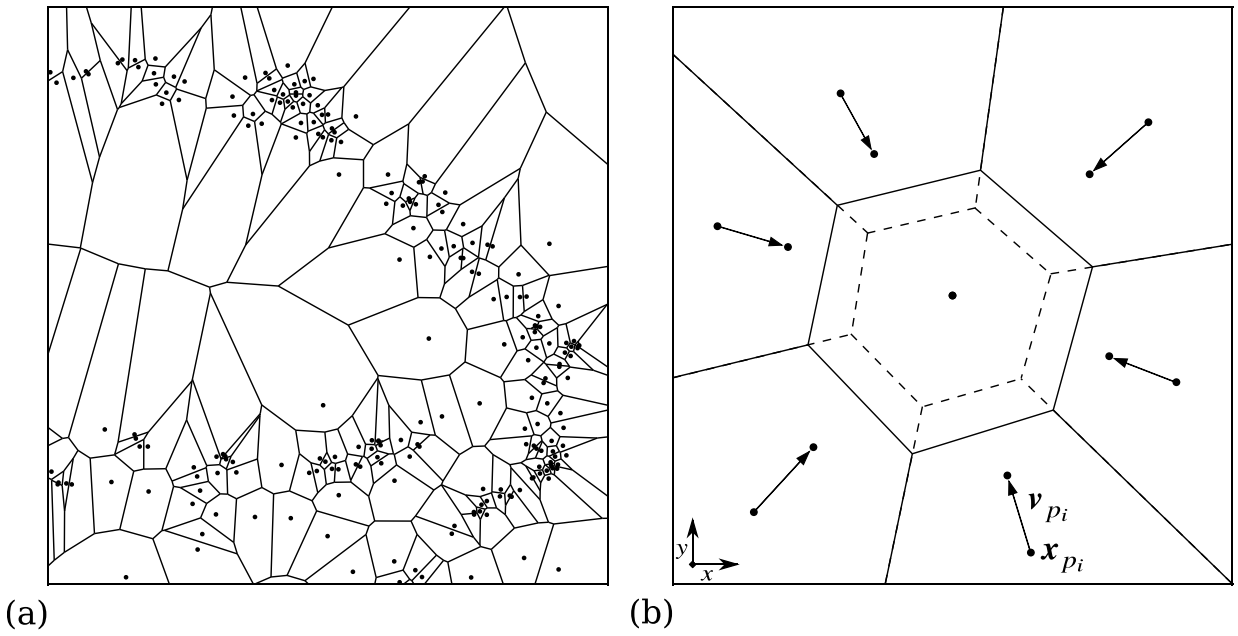

Fig. 1. (a) Voronoi tessellation in 2D for a cluster of particles. (b) Example of the motion of a two-dimensional modified Voronoi tessellation at two subsequent time instants for a converging cluster. The solid line corresponds to the time step t^k and the dashed line to t^{k+1}.

in the simulation suite because of their importance in determining the equilibrium distribution of particles by counteracting the near-wall accumulation due to turbophoresis (Li et al., 2001; Vreman, 2007).

All simulation cases use the same flow domain and boundary conditions. The channel dimensions are $4\pi\delta \times 2\delta \times (4/3)\pi\delta$ (where $\delta = 2$ cm), with periodic boundary conditions in x and z, and smooth, no-slip walls in y. A grid resolution of $[N_x, N_y, N_z] = [280, 140, 140]$ was used to resolve the fluid turbulence at reasonable computational cost. The computational grid is stretched in the wall-normal direction using the hyperbolic tangent stretching function from Bose (2012), Eq. (2).11. The grid is uniform in homogeneous directions. For the single-phase baseline case, there are 23 grid points below $y^+ = 10$, and the centreline grid resolution is $[\Delta x^+, \Delta y^+, \Delta z^+] = [10.5, 9.1, 7.0]$.

A constant time step was used for each simulation case, based on the viscous stability condition, such that for all cases $\Delta t^+ \leq 9 \times 10^{-3}$. For the statistics reported in the following sections, all simulation cases were run until a steady state was reached. Then, simulations were continued for a minimum of 5 flow-through times. Eulerian statistics of time-averaged quantities were obtained by averaging continuously throughout this period, as well as over homogeneous directions. The PDFs of divergence, curl, and helicity were computed from 10 snapshots evenly distributed during the averaging time. Eulerian PDFs were obtained using the same differential operators and grid as the simulation. Lagrangian PDFs were computed with the tessellation technique described in Section 2.2.

2.2. Tessellation and differential analysis of the particle velocity

2.2.1. Voronoi and delaunay tessellation

The Delaunay tessellation of the particle positions represents the graph such that no particles are inside the circumscribed sphere of any cells. The dual graph of the Delaunay tessellation defines the Voronoi tessellation, which has the property that all points inside are closer to the particle than to the other particles. Fig. 1(a) shows a particle cluster and the corresponding Voronoi tessellation. We can observe that when the particles are grouped together the Voronoi cell is small, and when the particles are dispersed the Voronoi cell is large. For this reason, small Voronoi cells are characteristic of clusters, and large cells are characteristic of voids. In the following, we use the modified Voronoi tessellation defined in Maurel-Oujia et al. (2023) which uses the centre of gravity of the Delaunay cell to define the vertices of the dual cell C_p, instead of using the circumcentre of the Delaunay cell as done for the Voronoi tessellation. It was shown by Maurel-Oujia et al. (2023) that this construction improves the stability of the numerical method when computing divergence and curl. For computing the 3D tessellation (Aurenhammer, 1991), we apply the Quickhull algorithm (Barber et al., 1996) to the particle positions. In order to take into account the domain walls, the cells corresponding to particles close to the wall and belonging to the convex hull are altered. Each altered cell is composed of the vertices of the cell generated by the modified Voronoi tessellation to which we add the orthogonal projection of these vertices onto the wall. This procedure also prevents degenerated cells, i.e. cells whose particle lies outside its tessellation cell. Note that the number of these modified cells is extremely small: their contribution to the PDFs is of the order of 10^{-6}–10^{-7}.

2.2.2. Divergence, curl, and helicity

To compute the divergence of the particle velocity $\mathcal{D}(\boldsymbol{v}_p)$, following the lines of Oujia et al. (2020), Maurel-Oujia et al. (2023), we first compute the local number density averaged over a cell C_p, which is the inverse of the cell volume. Particles satisfy the conservation equation of the number density n: $D_t n = -n\nabla \cdot \boldsymbol{v}$, where $D_t = \partial_t + \boldsymbol{v} \cdot \nabla$ is the Lagrangian derivative. Considering two subsequent time instants t^k and $t^{k+1} = t^k + \Delta t$ of the modified Voronoi tessellation with time step Δt, we can determine the volume change. Thus we obtain the divergence of the particle velocity as

$$\mathcal{D}(\boldsymbol{v}_p) = -\frac{1}{n} D_t n \approx \frac{1}{2\Delta t}\left(\frac{1}{V_p^{k+1}} + \frac{1}{V_p^k}\right)(V_p^{k+1} - V_p^k), \tag{5}$$

where V_p^k is the modified Voronoi cell volume at t^k. A small timestep is used to ensure that the divergence is calculated accurately. Across all the simulation cases, the timesteps used lie in the range $4 \times 10^{-4} < \Delta t^+ < 8 \times 10^{-4}$. Fig. 1(b) shows the dynamics of a modified Voronoi cell at two subsequent time instants. We can observe the decrease of the volume of the cell in the case where the particles are compressed, which corresponds to a convergence of the particle velocity (negative divergence).

Similarly, the curl of the particle velocity can be defined by computing the circulation of the velocity field of particles over a cell C_p.

Each component of the curl can also be expressed as the divergence of the velocity which has been projected on the plane orthogonal to the component and rotated in a direction $-\pi/2$ around the vector normal to the plane (Oujia et al., 2020; Maurel-Oujia et al., 2023). That is, the curl of the particle velocity $C(\boldsymbol{v}_p)$ is obtained by

$$\boldsymbol{C}(\boldsymbol{v}_p) = \begin{pmatrix} C_x(\boldsymbol{v}_p) \\ C_y(\boldsymbol{v}_p) \\ C_z(\boldsymbol{v}_p) \end{pmatrix} = \begin{pmatrix} \mathcal{D}\left(-\boldsymbol{v}_{p,x}^{\perp}\right) \\ \mathcal{D}\left(-\boldsymbol{v}_{p,y}^{\perp}\right) \\ \mathcal{D}\left(-\boldsymbol{v}_{p,z}^{\perp}\right) \end{pmatrix}, \tag{6}$$

where $\boldsymbol{v}_{p,x}^{\perp} = \boldsymbol{L}_x\boldsymbol{v}_p$, $\boldsymbol{v}_{p,y}^{\perp} = \boldsymbol{L}_y\boldsymbol{v}_p$, and $\boldsymbol{v}_{p,z}^{\perp} = \boldsymbol{L}_z\boldsymbol{v}_p$. Here, $\boldsymbol{L}_x$, $\boldsymbol{L}_y$ and $\boldsymbol{L}_z$ are the rotation matrices around the x, y, and z axes, respectively, which are defined as

$$\boldsymbol{L}_x = \begin{pmatrix} 0 & 0 & 0 \\ 0 & 0 & -1 \\ 0 & 1 & 0 \end{pmatrix}, \boldsymbol{L}_y = \begin{pmatrix} 0 & 0 & 1 \\ 0 & 0 & 0 \\ -1 & 0 & 0 \end{pmatrix}, \text{ and } \boldsymbol{L}_z = \begin{pmatrix} 0 & -1 & 0 \\ 1 & 0 & 0 \\ 0 & 0 & 0 \end{pmatrix}. \tag{7}$$

Thus, each component of the curl can be obtained by computing the volume of the cells at time t^k, and the volume of the cells advected by each velocity $-\boldsymbol{v}_{p,x}^{\perp}$, $-\boldsymbol{v}_{p,y}^{\perp}$ and $-\boldsymbol{v}_{p,z}^{\perp}$, and then applying them to Eq. (5). For more details and a thorough validation in the case of a one-way coupled particle-laden isotropic turbulence, we refer to Maurel-Oujia et al. (2023).

Having access to the curl of the particle velocity, the helicity of the particle velocity can be computed. Helicity is defined as the scalar product of vorticity and velocity, and yields geometrical information on the alignment of both vector quantities. Geometrical statistics can thus be computed and swirling motion of particle clouds can be quantified. The relative helicity of the particle velocity is defined as

$$\mathcal{H}(\boldsymbol{v}_p) = \frac{\boldsymbol{v}_p \cdot \boldsymbol{C}(\boldsymbol{v}_p)}{\|\boldsymbol{v}_p\|_2 \ \|\boldsymbol{C}(\boldsymbol{v}_p)\|_2}, \tag{8}$$

and yields the cosine of the angle between the two vectors at each particle position. The range lies between -1 and $+1$, corresponding respectively to anti-alignment and alignment of vorticity and velocity, i.e. strong swirling motion. Two-dimensional motion corresponds to values of 0, reflecting orthogonality between vorticity and velocity.

In channel flow, there is both a mean velocity and mean shear, i.e. $\boldsymbol{v}_p = V_x\boldsymbol{e}_x + \boldsymbol{v}_p'$ and $\boldsymbol{C} = S_z\boldsymbol{e}_z + \boldsymbol{C}'$, where $S_z = dV_x/dy$. In addition, symmetry in the wall-normal direction must be accounted for. Therefore, when computing statistics of the z-component of curl, C_z is used in the bottom half of the channel, and its negative is used in the top half. The data are lumped together to compute PDFs. Accounting for the mean velocity and shear, helicity can be expressed as $\mathcal{H} = \frac{V_xC_x' + S_zv_z' + \boldsymbol{v}_p'\cdot\boldsymbol{C}'}{\|V_x\boldsymbol{e}_x + \boldsymbol{v}_p'\|_2 \|S_z\boldsymbol{e}_z + \boldsymbol{C}'\|_2}$. This implies that in channel flow, important contributions to helicity come from the alignment of vorticity fluctuations with the streamwise mean velocity, and the alignment of velocity fluctuations with the mean shear.

2.3. Fourier spectra of number density fluctuations

The Fourier spectra of number density fluctuations are calculated for two-dimensional slices in each layer based on the method in Matsuda et al. (2014). In this method, an analytical Fourier transform is applied to the particle number density in the sliced layer, which is given by

$$n_s(\boldsymbol{x}) = \frac{1}{n_{s0}} \sum_{m=1}^{N_{ps}} \delta_{\text{Dirac}}\left(\boldsymbol{x} - \boldsymbol{x}_p^{(m)}\right), \tag{9}$$

where N_{ps} is the number of particles in the sliced layer. The mean number density in the sliced layer is used for the scaling factor n_{s0}. The two-dimensional discrete Fourier transform of $n_s(\boldsymbol{x})$ is then given by

$$\hat{n_s}(\boldsymbol{k}) = \frac{1}{N_{ps}} \sum_{m=1}^{N_{ps}} \exp\left(-i\boldsymbol{k}\cdot\boldsymbol{x}_p^{(m)}\right), \tag{10}$$

where $\boldsymbol{k}$ is the two-dimensional wavenumber vector, i.e., $\boldsymbol{k} = (l_1\Delta k_x, 0, l_2\Delta k_z)$ for integers l_1 and l_2, $\Delta k_x\delta = 1/2$, and $\Delta k_z\delta = 3/2$. The number density spectrum $E_n(k)$ is given by

$$E_n(k) = \frac{1}{\Delta k} \sum_{k-\Delta k/2 \le |\boldsymbol{k}| < k+\Delta k/2} \hat{\Phi}(\boldsymbol{k}), \tag{11}$$

where Δk is the wavenumber interval (3/2). $\hat{\Phi}(\boldsymbol{k})$ is the spectral density function given by $\hat{\Phi}(\boldsymbol{k}) = \hat{n_s}(\boldsymbol{k})\hat{n_s}^*(\boldsymbol{k})$. By substituting (10), $\hat{\Phi}(\boldsymbol{k})$ is given by

$$\hat{\Phi}(\boldsymbol{k}) = \left[\frac{1}{N_{ps}} \sum_{m=1}^{N_{ps}} \cos\left(\boldsymbol{k}\cdot\boldsymbol{x}_p^{(m)}\right)\right]^2 + \left[\frac{1}{N_{ps}} \sum_{m=1}^{N_{ps}} \sin\left(\boldsymbol{k}\cdot\boldsymbol{x}_p^{(m)}\right)\right]^2 - \frac{1}{N_{ps}}. \tag{12}$$

The third term on the right-hand side of (12) is introduced to remove the Poisson noise in the spectrum. The two dimensional Fourier spectrum of particle number density can be also defined by

$$E_{n,2D}(k_x, k_z) = \frac{\hat{\Phi}(\boldsymbol{k})}{\Delta k_x \Delta k_z} \tag{13}$$

Thus the wavenumber distribution of the particle number density can be studied in the different planes of motion and the flow anisotropy can be assessed.

2.4. Collision rate

The collision rate is calculated by counting the number of collisions that occur in a given flow region (viscous sublayer, buffer layer, and log layer), and dividing by the runtime of the simulation and the volume of the region. Initialising the simulation from each of the ten snapshots used in this study for the Lagrangian statistics, collisions were counted for the subsequent 1,000 timesteps. Averaging the ten integration periods together, this amounts to at least 50 viscous timescales for each simulation case.

Using the spherical formulation proposed by Wang et al. (2000), the particle collision rate N_c can be expressed as

$$N_c = \pi D_p^2 n^2 g(D_p) \langle |w_r| \rangle, \tag{14}$$

in which $g(D_p)$ is the radial distribution function at contact, and $\langle |w_r| \rangle$ denotes an ensemble average of the relative radial velocity between particles. N_c is non-dimensionalised by the number density averaged over the appropriate flow region squared and the particle diameter squared, and the friction velocity is used as a representative velocity scale.

$$\widetilde{N}_c = \frac{N_c}{n^2 D_p^2 u_\tau} = \pi g(D_p) \langle |w_r^+| \rangle. \tag{15}$$

This non-dimensionalisation depends only on the radial distribution function and distribution of relative velocities, so it conveys how likely particles are to collide irrespective of the number density.

3. Results

In this section, we first present Eulerian statistics of the fluid-phase channel flow data and then present the Lagrangian particle statistics. We analyse results of divergence, curl, and helicity of the particle velocity as a function of Stokes number St^+, mass loading ϕ_0, and in different flow regions. Here, the channel flow is broken up into three regions based on the wall-normal distance. For this purpose, the viscous sublayer is defined as the region $y^+ = [0, 5]$, the buffer layer is defined as $y^+ = [5, 30]$ and the logarithmic (log) layer is defined as $y^+ = [50, Re_\tau]$. Strictly speaking, this definition includes the outer layer as well, but the particle clustering observed in these two regions is fairly similar, as evidenced by similarities in PDFs of Voronoi volumes in Nilsen et al. (2013).

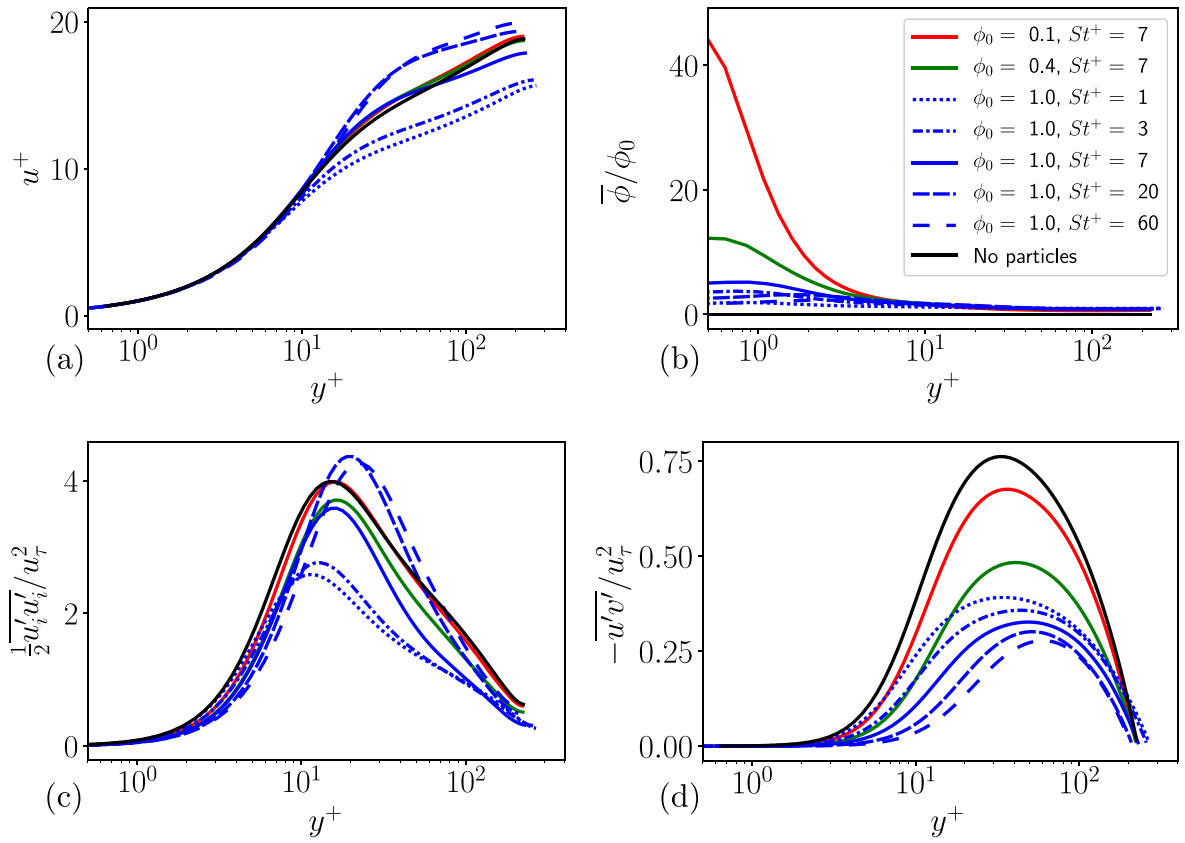

Fig. 2. (a) Mean streamwise fluid velocity, u^+, as a function of wall-normal distance, y^+, for various mass loadings and Stokes numbers, as well as without particles. (b) Local mean mass loading. (c) Fluid phase turbulent kinetic energy (TKE). (d) Fluid phase Reynolds shear stress ($\overline{u'v'}$). The legend in (b) applies to all sub-figures.

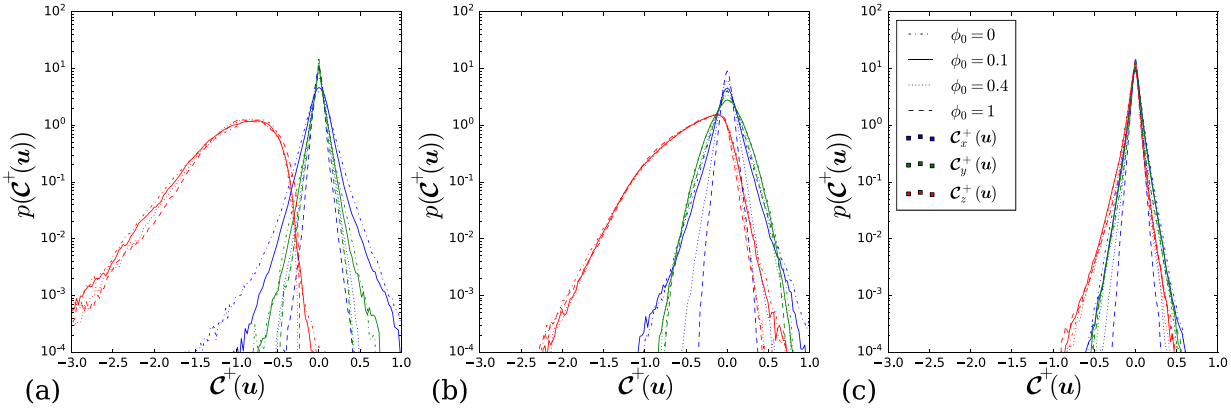

Fig. 3. PDF of fluid vorticity, normalised by the viscous time scale, for different mass loadings with $St^+ = 7$, in the (a) viscous sublayer, (b) buffer layer and (c) log layer. The line colour indicates the component of the vorticity, and the line style indicates the mass loading.

3.1. Carrier fluid statistics

In four-way coupled turbulent channel flow, particles alter the fluid velocity, both in the mean and fluctuations. In addition, particles tend to accumulate near the channel walls due to turbophoresis (Reeks, 1983; Marchioli and Soldati, 2002). Fig. 2 shows the degree of these changes in time-averaged quantities, depending on the mass loading and Stokes number. Increasing mass loading decreases the slope of u^+ in the log layer, due to the additional inertia added by particles. Stokes number has less of an effect on the log layer slope, but adds an offset, due to thickening of the viscous sublayer. Fig. 2(b) shows the local mass loading normalised by the total mass loading, which peaks very close to the wall due to turbophoresis. As mass loading is increased, collisions are more frequent, disrupting the tendency to accumulate near the wall. At lower values of ϕ_0, this results in stronger gradients in mass loading through the viscous sublayer, and a greater difference in mass loading from near-wall to centreline. In terms of turbulence, the fluid phase turbulent kinetic energy (TKE), shown in 2(c), is attenuated slightly as mass loading is increased, and the fluid Reynolds stress, shown in 2(d), is attenuated strongly. This is due to an attenuation of the pressure-strain term in the TKE budget, which prevents transfer of energy from streamwise fluctuations to other directions, making the Reynolds stress more anisotropic (Li et al., 2001). Within the same mass loading ($\phi_0 = 1$), the effect of increasing Stokes number is to decrease the fluid phase Reynolds stress and increase the fluid-phase TKE up to a point. This is due to the enhancement of streamwise velocity fluctuations and attenuation of wall-normal fluctuations. Lee and Lee (2015) also observed the attenuation in Reynolds stress as St^+

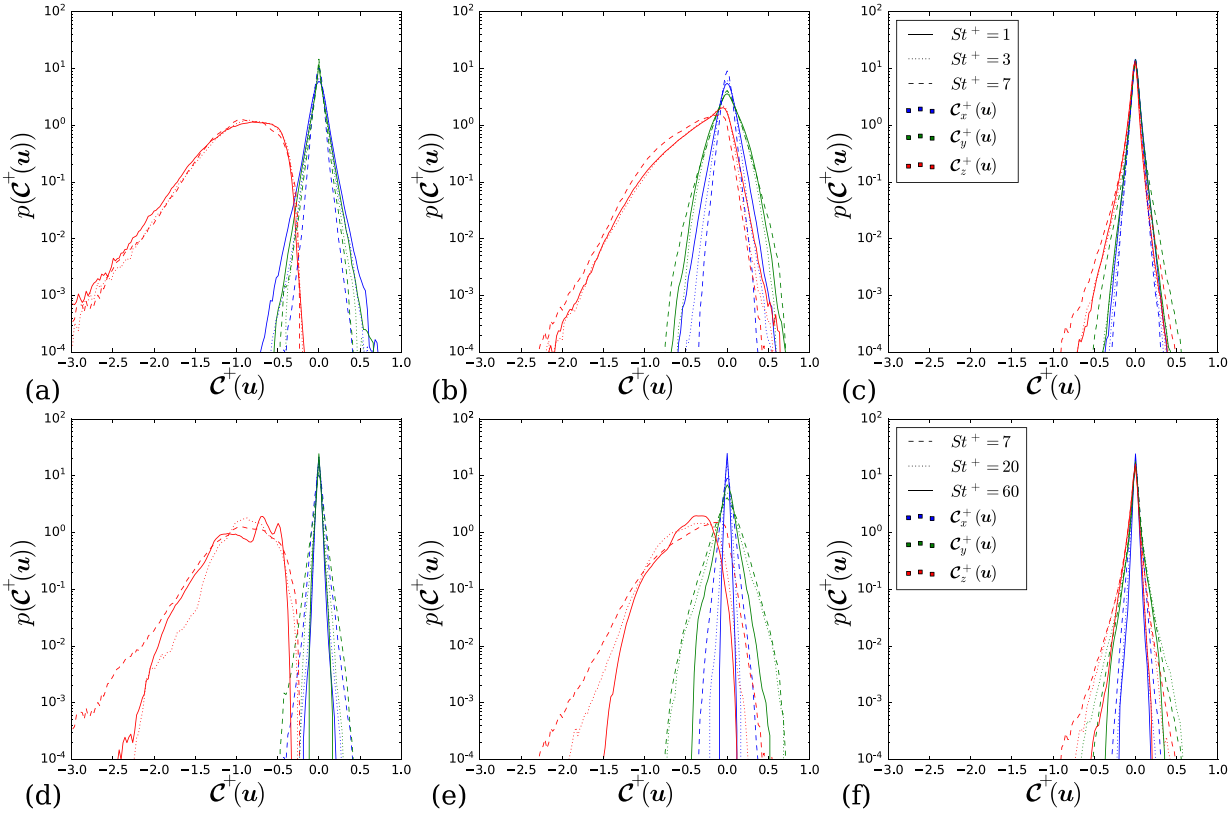

Fig. 4. PDF of fluid vorticity, normalised by the viscous time scale, for a range of Stokes numbers with $\phi_0 = 1$. Data for small Stokes numbers: (a) viscous sublayer, (b) buffer layer and (c) log layer. Data for large Stokes numbers: (d) viscous sublayer, (e) buffer layer and (f) log layer. The line colour indicates the component of the vorticity, and the line style indicates the Stokes number.

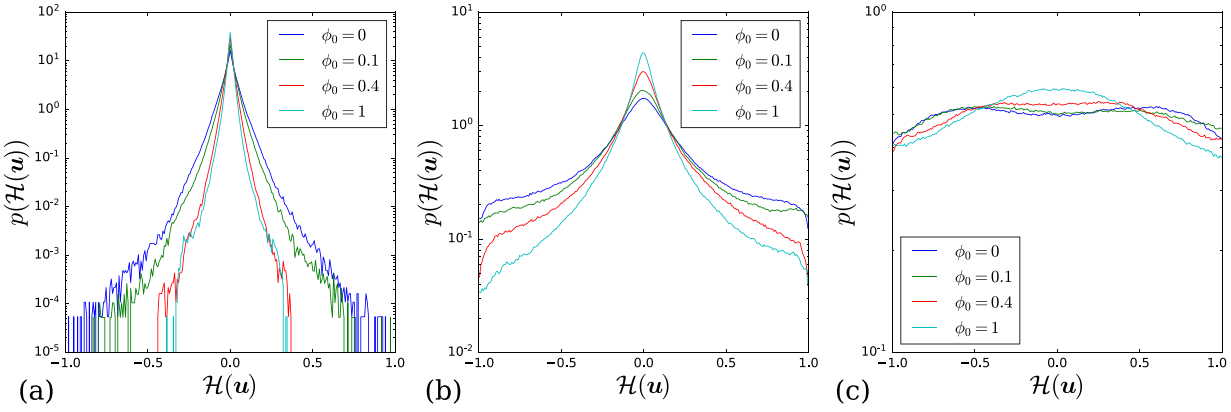

Fig. 5. PDF of fluid relative helicity for various mass loadings with $St^+ =$, in the (a) viscous sublayer, (b) buffer layer and (c) log layer. Note that the y-axis ranges for each PDF are different.

is increased at $\phi_0 = 0.3$, but not the enhancement in streamwise velocity fluctuations observed here (at $\phi_0 = 1$). Zhao et al. (2013) observed enhancement in streamwise velocity fluctuations with increasing St^+, but mass loading was increased at the same time. Therefore, it seems that the degree of enhancement or attenuation in TKE may be dependent on the specific combination of Stokes number and mass loading.

Next, we consider the distribution of the fluid vorticity in Fig. 3, which shows PDFs of the three components of the fluid vorticity normalised by the viscous time scale, $\mathcal{C}^+ = \tau_{visc}\mathcal{C}$, in the different flow regions, for the different mass loadings considered, including the no particle case ($\phi_0 = 0$). This shows the influence of the particle feedback force, which increases in proportion to mass loading. In the viscous sublayer - Fig. 3(a) - the z-component of curl is centred around -1 due to the mean shear which dominates this region. The distribution of $\mathcal{C}_z^+$ is also highly skewed, and events with $\mathcal{C}_z^+ > 0$, i.e. temporary reversal of mean shear, are extremely unlikely. The $\mathcal{C}_x^+$ and $\mathcal{C}_y^+$ distributions are nearly symmetric, as expected from the flow geometry. Moving towards the log layer, the distribution of $\mathcal{C}_z^+$ becomes more symmetric, and the three components more similar, indicating the greater isotropy of turbulence in the log layer. Neither $\mathcal{C}_y^+$ nor $\mathcal{C}_z^+$ is significantly affected by mass loading. However, $\mathcal{C}_x^+$, which corresponds to the elongated quasi-streamwise vortices found in the near-wall region of channel flow (Robinson, 1991), is strongly attenuated as ϕ_0 increases. While a small degree of anisotropy is expected in the log layer for channel flow at low Reynolds number (Andersson et al., 2015), the extreme attenuation of $\mathcal{C}_x^+$ relative to the other two components is a unique feature of particle-laden wall turbulence. The weakening of quasi-streamwise structures by particles (Dritselis and Vlachos, 2008; Lee

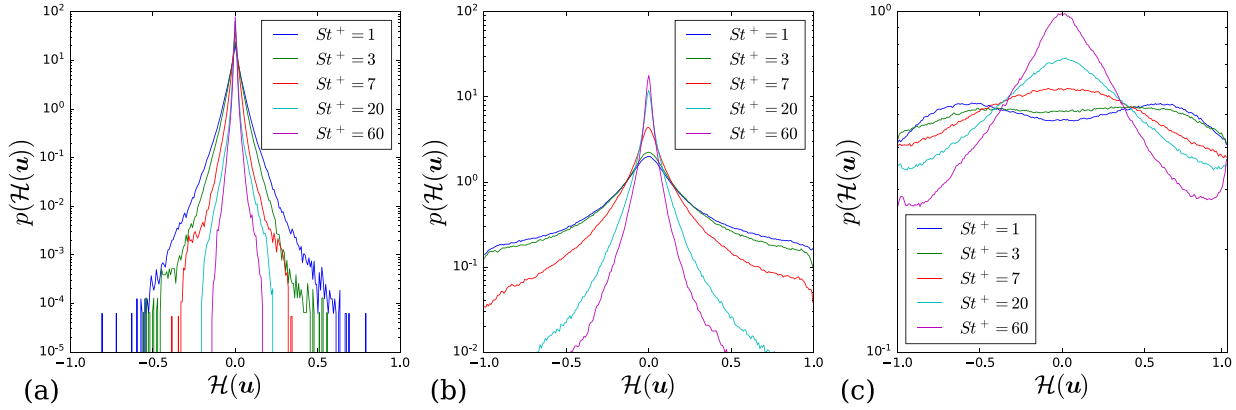

Fig. 6. PDF of fluid relative helicity for various Stokes numbers with $\phi_0 = 1$, in the (a) viscous sublayer, (b) buffer layer and (c) log layer. Note that the y-axis ranges for each PDF are different.

and Lee, 2015) and of coherent structures in general (Vreman, 2007) has been observed in prior studies. As ϕ_0 is increased, particle-laden wall turbulence becomes more anisotropic, dominated by streamwise velocity fluctuations (Li et al., 2001). These streamwise velocity fluctuations can contribute to vorticity fluctuations in C_y^+ and C_z^+, but not C_x^+, resulting in the selective attenuation.

The effect of St^+ on the PDFs of fluid vorticity is shown in Fig. 4(a–c) for small St^+ and Fig. 4(d–f) for large St^+. For small St^+, the variation in St^+ has little effect on C_y^+, and C_x^+ is attenuated more as St^+ is increased, much like the variation in mass loading. This can again be explained by the increasing anisotropy of the Reynolds stress with St^+, which was also noted by Lee and Lee (2015). C_z^+ variance is somewhat enhanced in the log layer, perhaps due to the stronger streamwise velocity fluctuations with increasing St^+. As St^+ increases beyond $St^+ = 7$, all three curl components are attenuated, and C_z^+ is preferentially attenuated at negative values, resulting in a narrower, less skewed distribution as particle motions (and the drag forces particles exert) become more random, and less determined by eddies. The effect of this change on the fluid phase is to weaken rotational motion (i.e. eddies) at large Stokes numbers.

Finally, the fluid-phase relative helicity distributions are plotted in Fig. 5 for the effect of ϕ_0 and Fig. 6 for the effect of St^+. The helicity distributions are all symmetric with zero mean due to the problem geometry, but they are strongly affected by flow region. As previously noted by Rogers and Moin (1987), the probability of having zero helicity is highest in the viscous sublayer because the near-wall vorticity is dominated by the mean shear ($d\bar{u}/dy$), which is orthogonal to the streamwise velocity. The helicity distribution becomes flatter with increasing wall distance, i.e. the flow becomes more three-dimensional, exhibiting swirling motions absent near the wall. Across all three layers, the effect of increasing the mass loading or Stokes number is to make the flow more two-dimensional. In the viscous sublayer and buffer layer, this can be interpreted as a consequence of the low-speed streaks becoming more stable and persistent, due to two-way coupling. In the log layer, for sufficiently small ϕ_0 and St^+, there are two peaks at moderate values of helicity. Previous observations from HIT (Oujia et al., 2022) have shown peaks at $\mathcal{H}(\boldsymbol{v}_p) = \pm 1$ for small Stokes number, indicating a greater probability of swirl than non-swirl. The peaks at moderate values observed here may be due to the increased anisotropy of particle-laden wall turbulence, which limits how three-dimensional its coherent structures can be. However, we can conjecture that the curves obtained at $St^+ = 1$ and $\phi_0 = 0.1$ represent a transition from a concave to convex PDF, and that in channel flows with small enough St^+ and ϕ_0, and high enough Reynolds number, the curves would become convex as observed in Oujia et al. (2022).

3.2. Particle phase Lagrangian statistics

3.2.1. Influence of Stokes number

In this section we consider the effect of Stokes number on cluster dynamics by examining the particle velocity divergence, curl, and helicity for $St^+ = [1 - 60]$. It is important to underscore that all cases considered in this section have the same mass loading, $\phi_0 = 1$, at which strong two-way coupling effects between the phases, as well as significant changes in the turbulence anisotropy, are expected, as described in Section 3.1. We plot particle positions coloured by particle velocity divergence in Fig. 7 for $St^+ = 3$ and $St^+ = 60$. For $St^+ = 3$, shown in Fig. 7(a–c), the particles in the viscous sublayer organise into elongated chain-like structures (as found by many others, e.g. Marchioli and Soldati, 2002). The effect of particles on the low-speed streaks, as well as other flow structures, is shown with visualisations in Appendix. Clusters of particles with large positive and negative divergence are sparsely distributed, but the majority of particles have near-zero divergence (green colour), indicating that most particles are simply transported by the flow. In the clusters with non-zero divergence, positive and negative divergence are intermixed, suggesting collisions, which increase the energy of uncorrelated particle motions (Vance et al., 2006) and have been observed to increase in frequency closer to the wall (Li et al., 2001; Kuerten and Vreman, 2016). This fits with the observation of Fong et al. (2019) that the velocities of particles near the wall ($y^+ = [17 - 34]$ in their study) have a stronger uncorrelated component relative to those in the centreline.

Thin, elongated void regions, indicated by white space, appear between the particle streaks. In the buffer layer, clusters of particles with negative and positive divergence are more densely distributed, but they are less elongated. The more intense convergence/divergence in the buffer layer is likely due to the increased strength of velocity fluctuations there, as shown in Fig. 2(c). In the log layer, the density of clusters with non-zero divergence is decreased, and their structures are less directional, bearing a strong resemblance to previous results in HIT for small Stokes numbers (Oujia et al., 2020). For $St^+ = 60$, shown in Fig. 7(d–f), the particle distributions and their velocity divergence are starkly different. The width of the streaky structures has greatly increased, matching the structure of the streamwise velocity field (Appendix, Fig. 26(d, e)). Throughout the layers, a much greater proportion of particles have non-zero divergence, indicating that particles are moving more independently of the surrounding fluid. Finally, we observe preferential concentration in the log layer for $St^+ = 60$, but only at large scales, as expected because of large particle inertia. In addition, there is a great deal of convergence/divergence intermixed throughout all layers for $St^+ = 60$, indicating a greater degree of spatially uncorrelated particle motions, as is expected for greater particle inertia (Février et al., 2005).

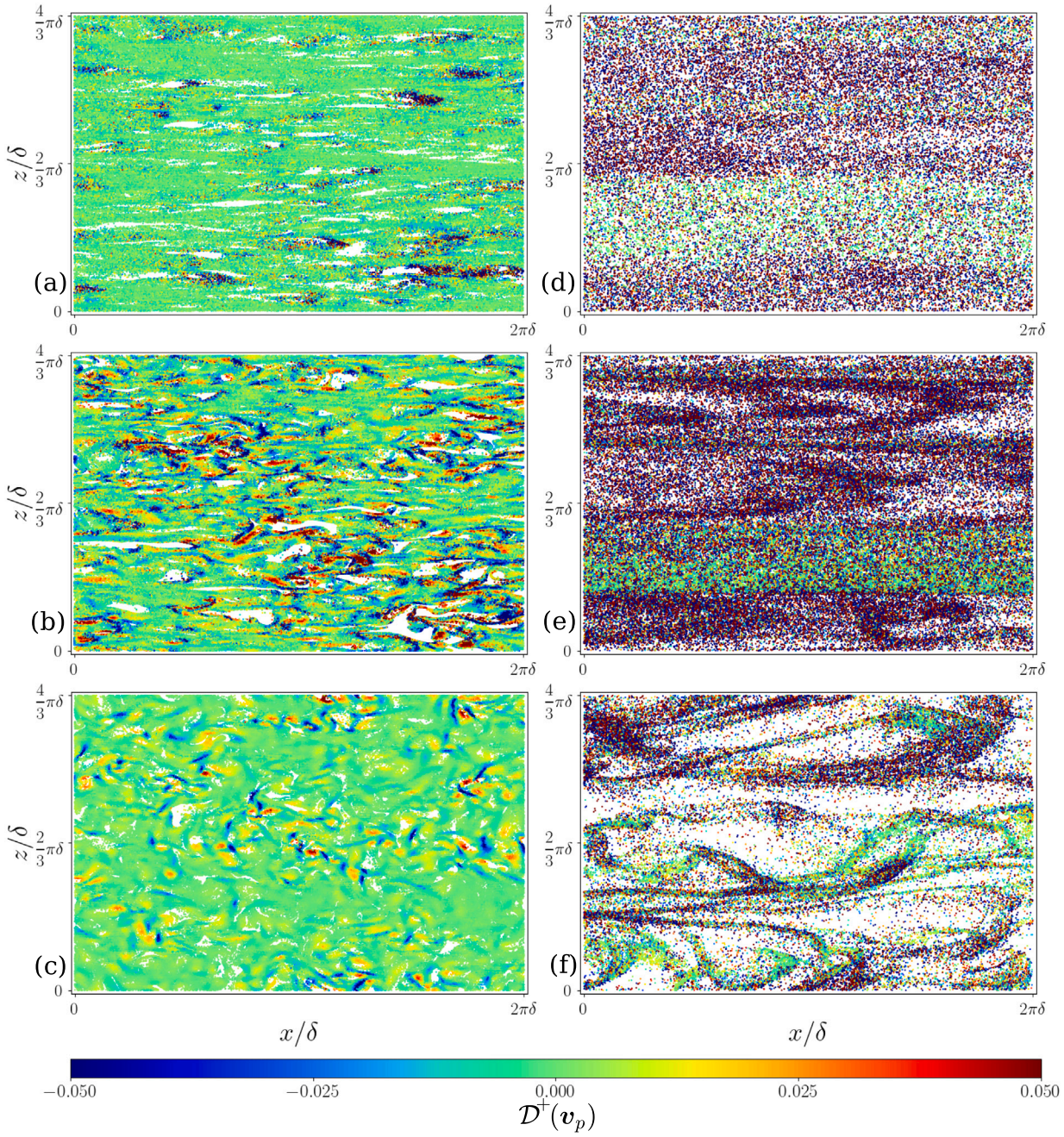

Fig. 7. Particle positions coloured by divergence in wall-parallel slices, for (a) viscous sublayer, $St^+ = 3$, $\phi_0 = 1$; (b) buffer layer, $St^+ = 3$, $\phi_0 = 1$; (c) log layer, $St^+ = 3$, $\phi_0 = 1$; (d) viscous sublayer, $St^+ = 60$, $\phi_0 = 1$; (e) buffer layer, $St^+ = 60$, $\phi_0 = 1$; (f) log layer, $St^+ = 60$, $\phi_0 = 1$. Divergence is normalised by the viscous time scale, and the colour bar is truncated to emphasise regions of zero divergence. Because of the difference in number density, thinner slices are used to visualise the $St^+ = 3$ data. The slices used for $St^+ = 3$ are $2.375 \leq y^+ < 2.625$, $11.375 \leq y^+ < 12.625$ and $99.375 \leq y^+ < 100.625$ for viscous sublayer, buffer layer and log layer, respectively. The slices used for $St^+ = 60$ are $2 \leq y^+ < 3$, $9.5 \leq y^+ < 14.5$ and $97.5 \leq y^+ < 102.5$ for viscous sublayer, buffer layer and log layer, respectively.

Fig. 8 shows snapshots of particles coloured by the magnitude of vorticity, using the same snapshots as in Fig. 7. In the viscous sublayer, this shows that the low-speed streaks where the divergence is near-zero correspond to low vorticity magnitude, due to the weaker shear in low speed streaks. Furthermore, the large values of divergence correspond to the regions of large vorticity magnitude. This trend applies to both small and large Stokes numbers, and continues into the buffer and log layers, suggesting that the rotational motion of particle clouds is a key contributor to divergence and convergence as particles are centrifuged out of eddies, or adjacent eddies bring clusters together. The vortical motion of particles in the log layer is similar to what has been observed for HIT in Oujia et al. (2022).

The helicity of the particle velocity is visualised in Fig. 9. Particle clusters in the log layer exhibit a greater alignment and anti-alignment of particle velocity and rotation, corresponding to dark red and dark blue particle regions, respectively. This confirms that particle clusters are swirling, i.e. their motion is helical. In contrast, in the viscous sublayer and the buffer layer helical motion is less present, since vorticity and velocity are more perpendicular there, resulting in two-dimensional motion of the particles. Stronger swirl is observed in Fig. 9(c) compared to Fig. 9(f), indicating that the particle motion becomes more two-dimensional as Stokes number is increased, even in the log layer.

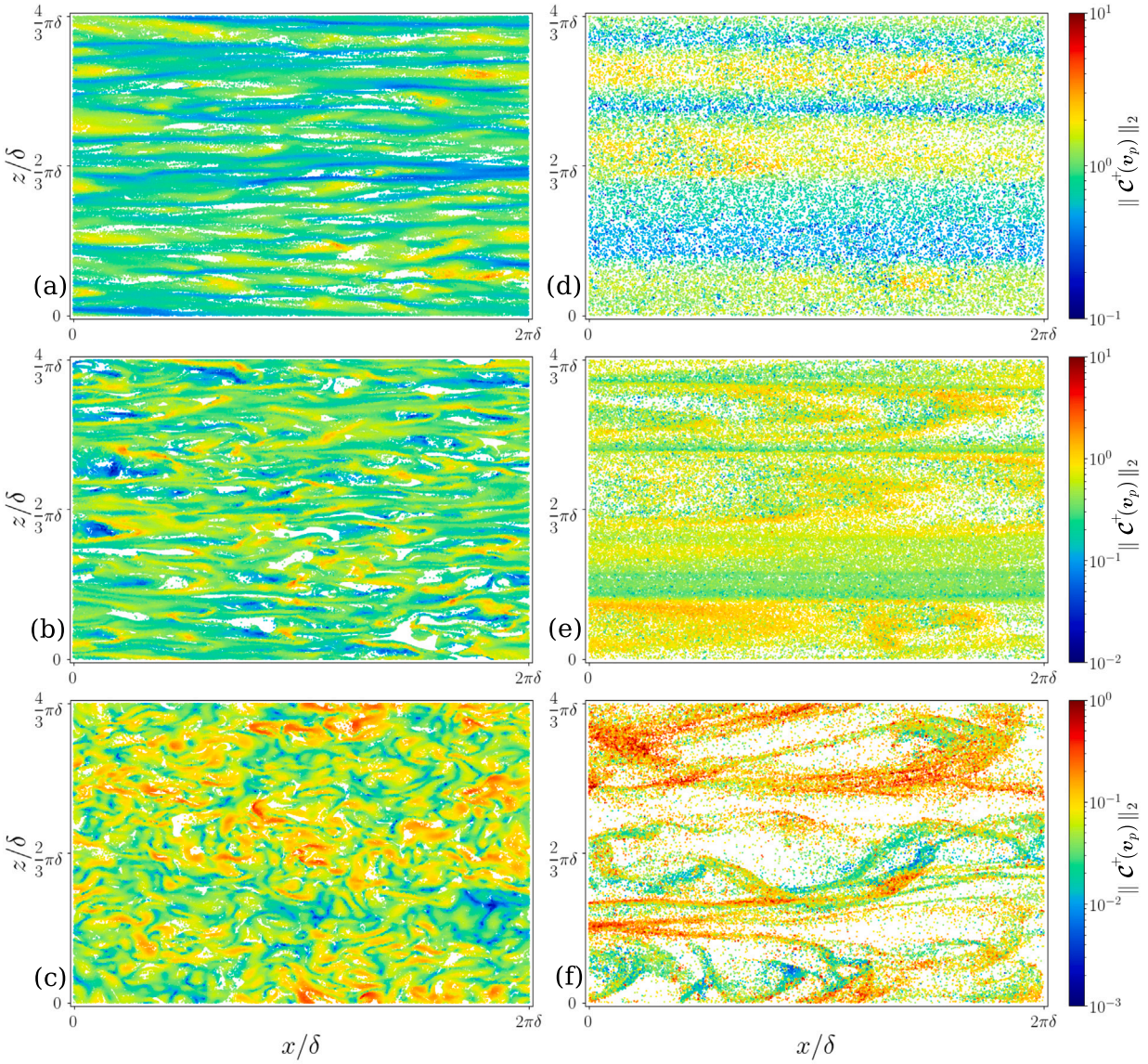

Fig. 8. Particle positions coloured by vorticity magnitude in wall-parallel slices, for (a) viscous sublayer, $St^+ = 3$, $\phi_0 = 1$; (b) buffer layer, $St^+ = 3$, $\phi_0 = 1$; (c) log layer, $St^+ = 3$, $\phi_0 = 1$; (d) viscous sublayer, $St^+ = 60$, $\phi_0 = 1$; (e) buffer layer, $St^+ = 60$, $\phi_0 = 1$; (f) log layer, $St^+ = 60$, $\phi_0 = 1$. Thickness of the layers used are defined in Fig. 7.

To characterise the presence of clusters and voids, Fig. 10 shows the PDFs of modified Voronoi volumes for each flow region and Stokes number normalised by the mean modified Voronoi volume within each layer $\overline{V}_{p,l}$. This normalisation (also used by Nilsen et al., 2013) is used because the particle number density is different within each layer due to turbophoresis, so this normalisation facilitates comparison with a random distribution within each layer. Across all flow regions, there is clear deviation from a random particle distribution with greater probabilities of both clusters and voids (small and large values of $V_{p,l}/\overline{V}_{p,l}$, respectively). At both very small and very large St^+, the distribution is closer to random than at intermediate St^+, where preferential concentration plays the greatest role. In general, the distribution of clusters in the viscous sublayer is closer to random than in other regions of the flow, except for $St^+ = 1$, in which the clusters are very close to random throughout the channel. This is in contrast to Nilsen et al. (2013), who found that the greatest departure from randomness in the viscous sublayer. We hypothesise that this difference is due to the effect of collisions, which cause the particle velocities to become less correlated (i.e. more random), and which become more frequent the closer a particle is to the wall (Li et al., 2001; Kuerten and Vreman, 2016). In addition, the significant two-way coupling at $\phi_0 = 1$ attenuates the turbulence that would otherwise preferentially concentrate particles into clusters and voids. Both collisions and two-way coupling omitted in Nilsen et al. (2013).

The large modified Voronoi volumes, i.e. voids, depart significantly from random in all layers, but especially in the viscous sublayer, where large, elongated voids between the streaks are present. The PDFs become noisy at their right tails due to a lack of samples. The distribution in the viscous sublayer is the noisiest because of the normalisation used. Particles are more densely packed in the viscous sublayer due to turbophoresis, so the average volume in the layer is smaller, shifting the curve to the right relative to other layers.

Fig. 11 shows the PDFs of particle velocity divergence for the different Stokes numbers, and Table 2 gives the variance and flatness values. The divergence data is normalised by the viscous timescale: $D^+ = \tau_{visc} D$. As St^+ is increased from a small value, the variance of the particle velocity divergence increases across flow regions, and the tails of the PDFs become heavier, as observed in HIT (Oujia et al., 2020). The very large values of flatness in Table 2 reflect the heavy tails and departure from Gaussianity due to extreme events. In addition,

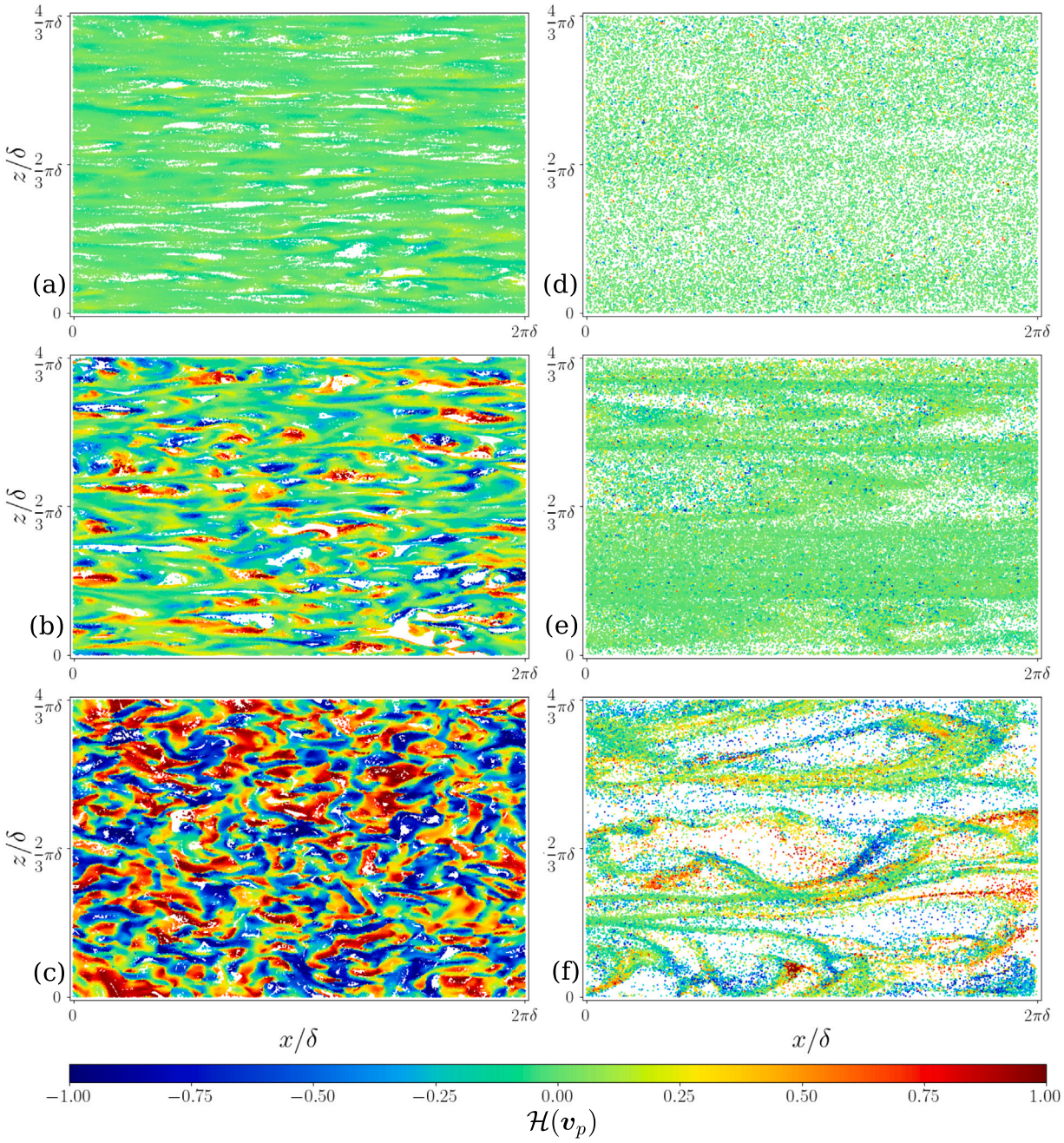

Fig. 9. Particle positions coloured by relative helicity in wall-parallel slices, for (a) viscous sublayer, $St^+ = 3$, $\phi_0 = 1$; (b) buffer layer, $St^+ = 3$, $\phi_0 = 1$; (c) log layer, $St^+ = 3$, $\phi_0 = 1$; (d) viscous sublayer, $St^+ = 60$, $\phi_0 = 1$; (e) buffer layer, $St^+ = 60$, $\phi_0 = 1$; (f) log layer, $St^+ = 60$, $\phi_0 = 1$. Thickness of the layers used are defined in Fig. 7.

we note that the flatness shows a non-monotonic trend, peaking at an intermediate Stokes number. At the tails, the PDFs become noisy, due to the rarity of particles with extreme values of divergence, which could be improved by averaging over additional flow snapshots. In the buffer layer, the variance is greatest, due to the strength of turbulent velocity fluctuations. This corresponds to the maximum in turbulent kinetic energy (TKE), which occurs in the range $10 \lesssim y^+ \lesssim 30$ for the flows considered here (see Fig. 2(c)). In the log layer and to a lesser extent the buffer layer, these changes eventually saturate: the increase in variance slows down and the flatness begins to decrease, because the TKE also saturates. This saturation occurs around $St^+ = 7$, which corresponds to $St_\eta^{\log} = 0.54$. Results from HIT show a similar transition at $St_\eta = 1$ (Oujia et al., 2020), which is remarkably close considering the differences in turbulence anisotropy, Reynolds number, and between one-way and four-way coupled simulations. By contrast, the variance of divergence continues to increase in the viscous sublayer, likely due to the increasingly ballistic motion of very heavy particles.

The particle collision rate is plotted in Fig. 12. In general, the collision rate is highest in the buffer layer, which is somewhat expected from the larger variance of the particle velocity in that region.[1] In the buffer layer and log layer, the collision rate increases with Stokes number, which reflects the trends observed by Wang et al.

[1] Kuerten and Vreman (2016) found that collisions monotonically increased close to the wall in their study of four-way coupled turbulent channel flow, using used a normalisation based on viscous scales, which is strongly influenced by number density, which increases near the wall due to turbophoresis.

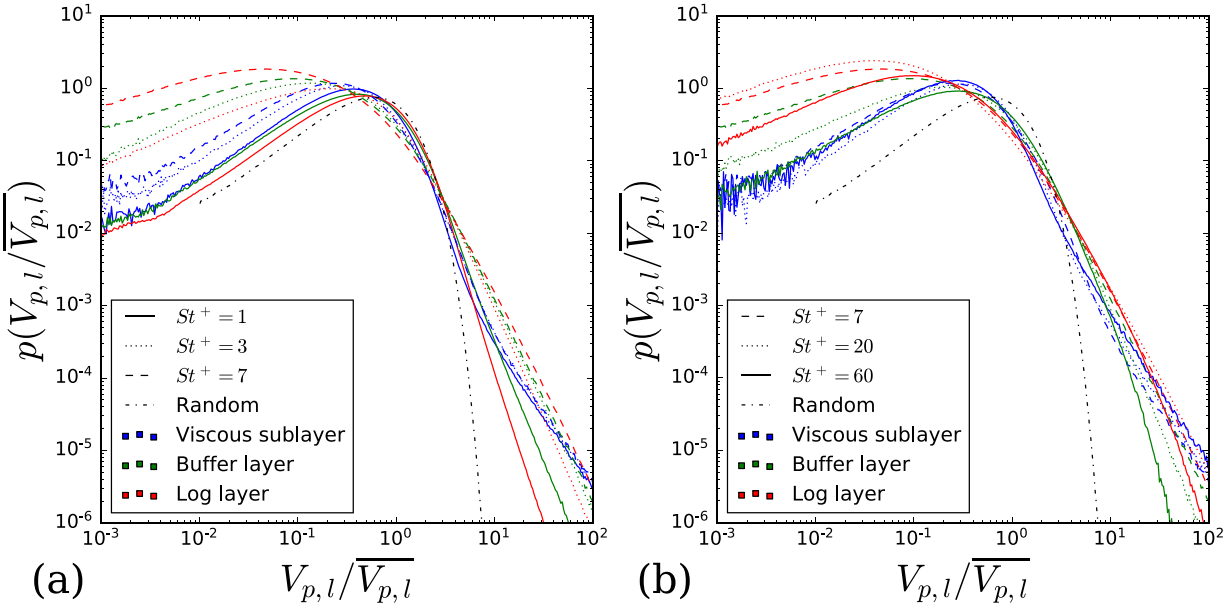

Fig. 10. PDF of modified Voronoi volume as a function of flow region and Stokes number, normalised by the mean modified Voronoi volume within each layer for (a) $St^+ = 1, 3, 7$; $\phi_0 = 1$, and (b) $St^+ = 7, 20, 60$; $\phi_0 = 1$. The dashed-dotted line represents the volume distribution for randomly distributed particles.

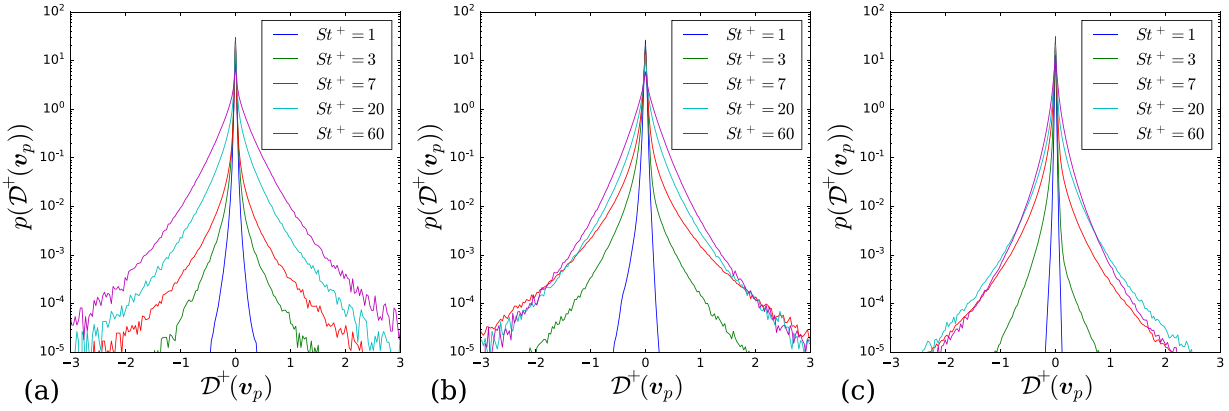

Fig. 11. PDF of particle velocity divergence, normalised by the viscous time scale, for various Stokes numbers with $\phi_0 = 1$, in the (a) viscous sublayer, (b) buffer layer, and (c) log layer.

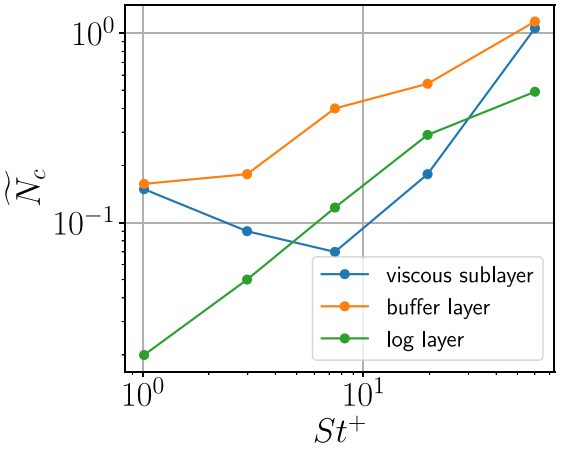

Fig. 12. Collision rate non-dimensionalised according to Eq. (15) for various Stokes numbers with $\phi_0 = 1$.

Table 2
Variance (left) and flatness (right) of the particle velocity divergence normalised by the viscous time scale for different layers and Stokes numbers St^+ with $\phi_0 = 1$.

St^+	Viscous	Buffer	Log	St^+	Viscous	Buffer	Log
1	7.93×10^{-5}	2.25×10^{-4}	2.23×10^{-5}	1	1.26×10^{2}	0.44×10^{2}	0.30×10^{2}
3	4.26×10^{-4}	1.88×10^{-3}	2.10×10^{-4}	3	9.91×10^{2}	2.73×10^{2}	8.39×10^{2}
7	1.79×10^{-3}	9.78×10^{-3}	2.47×10^{-3}	7	11.8×10^{2}	2.77×10^{2}	3.49×10^{2}
20	1.23×10^{-2}	1.91×10^{-2}	6.04×10^{-3}	20	0.77×10^{2}	0.51×10^{2}	1.07×10^{2}
60	4.35×10^{-2}	3.25×10^{-2}	7.06×10^{-3}	60	0.18×10^{2}	0.17×10^{2}	0.33×10^{2}

(2000). Surprisingly, collisions in the viscous sublayer appear to be suppressed at intermediate St^+. This may be a consequence of two-way coupling, since the local mass loading is higher in the viscous sublayer at intermediate St^+ (see Table 1).

Next, we address the particle velocity curl to characterise the vortical motion of clusters. Figs. 13(a–c) and 13(d–f) show PDFs of the three components of the curl of particle velocity in the different flow regions for small and large Stokes numbers, respectively. Like the divergence, curl has been normalised by the viscous timescale: $\boldsymbol{C}^+ = \tau_{visc}\boldsymbol{C}$. The particle-phase PDFs have heavier tails than their fluid counterparts in Fig. 4, indicating greater probability of extreme values, but they

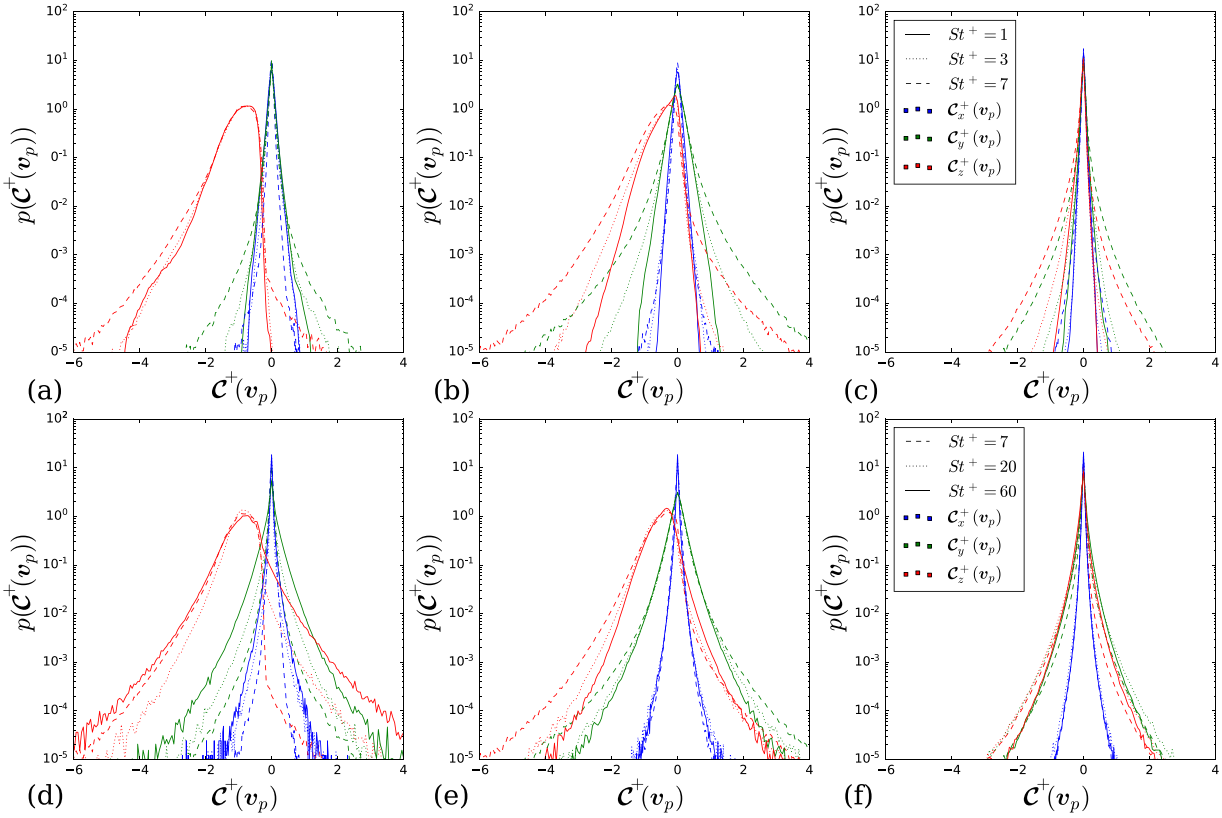

Fig. 13. PDF of particle velocity curl, normalised by the viscous time scale, for a range of Stokes numbers with $\phi_0 = 1$. Data for small Stokes numbers: (a) viscous sublayer, (b) buffer layer and (c) log layer. Data for large Stokes numbers: (d) viscous sublayer, (e) buffer layer and (f) log layer. The line colour indicates the component of the curl, and the line style indicates the Stokes number.

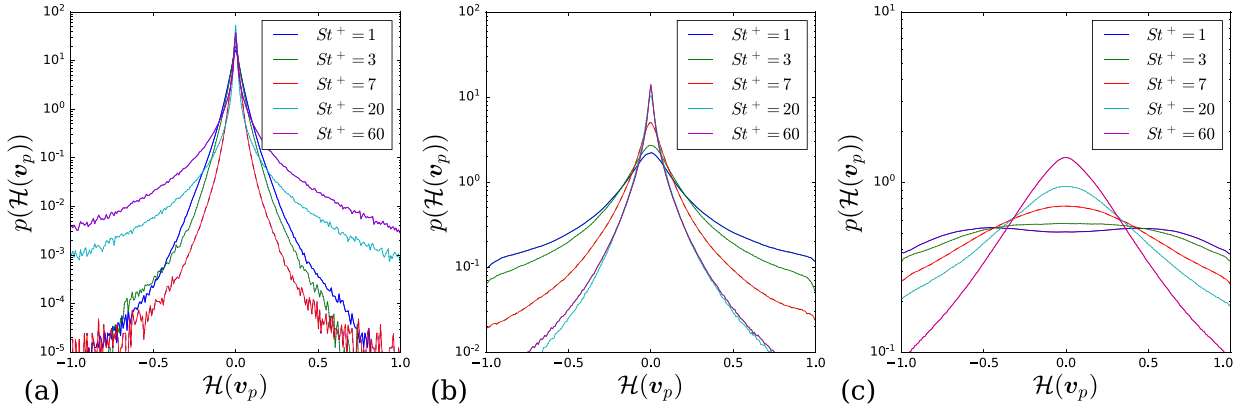

Fig. 14. PDFs of the relative helicity (cosine of the angle between particle velocity and vorticity) $\mathcal{H}(v_p)$ of the particles for various Stokes numbers with $\phi_0 = 1$, in the (a) viscous sublayer, (b) buffer layer, and (c) log layer. Note that the y-ranges differ by orders of magnitude.

show similar trends in terms of asymmetry and anisotropy, due to two-way coupling. The extreme values of vorticity are associated with short-lived, small-scale vortices. We hypothesise that such events are more likely in the particle phase because there is not a mechanism like viscosity to preferentially attenuate them, as there is in the fluid. Similar to divergence, the variance of particle velocity curl initially increases as St^+ increases, but then saturates in the log layer for larger St^+. This can be justified because intense fluctuations of fluid vorticity are short-lived, and the large particle inertia prevents the particles from following the streamlines of intense eddies. In the viscous sublayer, the effect on C_z^+ is particularly striking. As St^+ is increased, the distribution of C_z^+ remains offset with a mean value of -1, but it becomes more symmetrical, with significant distributions at $C_z^+ > 0$. This broadening of the PDF can be explained by the enhancement of the ballistic motions of inertial particles; with increasing inertia, the trajectories tend to become more independent of the streamlines of the carrier fluid.

Fig. 14 shows the PDFs of the particle helicity for various Stokes numbers. Similar to the fluid helicity, the particle helicity indicates that the motions of the particles become more two-dimensional approaching the wall. In the log layer, the distribution at large St^+ is concave, and it flattens as St^+ is decreased. The peaks at moderate values of helicity observed for $St^+ = 1$ suggest that the PDF may be transitioning from concave to convex, as observed in Oujia et al. (2022). Interestingly, in the viscous sublayer, a non-monotonic trend is observed, in contrast to the fluid helicity (Fig. 6). Initially the helicity distribution narrows as St^+ increases, but then it suddenly broadens, indicating that the particle motion is becoming more three-dimensional and independent of the fluid phase. Since the swirl of the

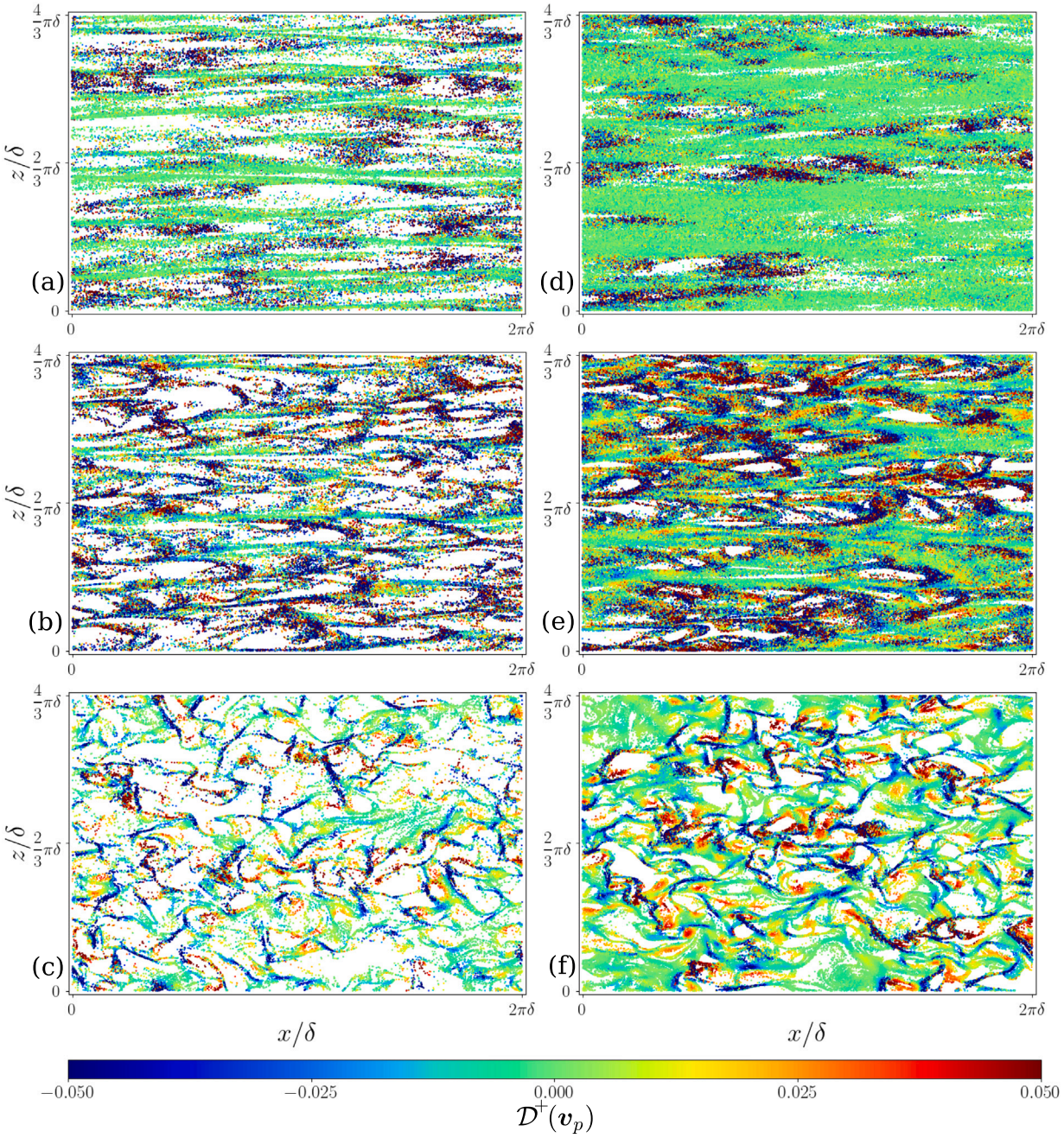

Fig. 15. Particle positions coloured by divergence in wall-parallel slices, for (a) viscous sublayer, $\phi_0 = 0.1$, $St^+ = 7$; (b) buffer layer, $\phi_0 = 0.1$, $St^+ = 7$; (c) log layer, $\phi_0 = 0.1$, $St^+ = 7$; (d) viscous sublayer, $\phi_0 = 0.4$, $St^+ = 7$; (e) buffer layer, $\phi_0 = 0.4$, $St^+ = 7$; (f) log layer, $\phi_0 = 0.4$, $St^+ = 7$. Divergence is normalised by the viscous time scale, and the colour bar is truncated to emphasise regions of zero divergence. The slices used for visualisation are $2 \leq y^+ < 3$, $9.5 \leq y^+ < 14.5$ and $97.5 \leq y^+ < 102.5$ for viscous sublayer, buffer layer, and log layer, respectively.

flow is reduced as St^+ increases, this increase in helicity in the viscous sublayer is likely due to the particle motion transitioning away from organised, but attenuated turbulent motion, to slightly more ballistic motion driven by particle inertia. Fig. 12 shows that the collision rate increases from $St^+ = 7$ to $St^+ = 60$, so it is possible that collisions may also play a role. The expected PDF for random ballistic particle motion is a uniform distribution, since all values of vorticity and velocity become equally likely.

Since the simulations used in this work are all four-way coupled, there is some uncertainty as to what extent the trends due to changing Stokes number are due collisions, the turbulence acting on the particles, or to the particle feedback force, which modulates the turbulence. However, given the striking similarities between the logarithmic layer and buffer layer results with previous studies of one-way coupled HIT (Oujia et al., 2020, 2022), it is expected that the main driver of the observed trends is the same preferential concentration mechanism present without the particle feedback force or collisions. Furthermore, the volume fractions of the simulations considered are small enough that it is unlikely that collisions are the dominant effect (Elghobashi, 1994). In the viscous sublayer, the effect of Stokes number on divergence, curl, and helicity is different than in the logarithmic layer, and so comparison with one-way coupled simulations would be illuminating to

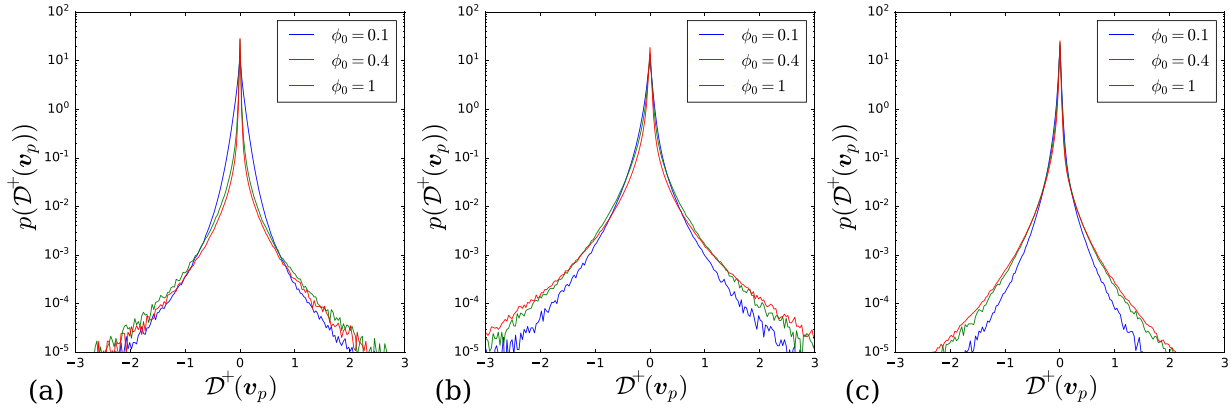

Fig. 16. PDF of particle velocity divergence, normalised by the viscous time scale, for three different mass loadings with $St^+ = 7$, in the (a) viscous sublayer, (b) buffer layer, and (c) log layer.

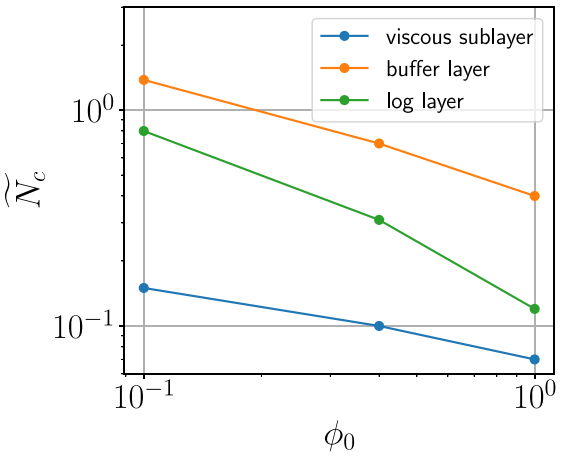

Fig. 17. Collision rate non-dimensionalised according to Eq. (15) for various mass loadings with $St^+ = 7$.

unpack the effect of the particle feedback force on clustering, rotation, and swirl in that region.

3.2.2. Influence of mass loading

Next, we examine the effect of mass loading on particle phase Lagrangian statistics. To gain a qualitative understanding of clustering and particle velocity divergence for different mass loadings, Fig. 15 shows particle positions coloured by divergence in wall-parallel slices. In the viscous sublayer, particles are organised into low-speed streaks with near-zero divergence, similar to the particles in Fig. 7(a), but the streaks are more distinct because the number density is lower. In the buffer layer, the streaky structures are still visible, but the prevalence of convergence and divergence is greatly increased. Finally, in the log layer, the clustering becomes similar to that of moderate Stokes number particles in HIT (Oujia et al., 2020). At larger mass loading, there is a greater proportion of zero-divergence particles, particularly in the viscous sublayer and buffer layers. As ϕ_0 is increased, the particles are more densely packed, but the structures remain qualitatively similar. Only $\phi_0 = 0.1, 0.4$ are shown, but the same qualitative trend continues to $\phi_0 = 1$.

PDFs of particle velocity divergence for each region are shown in Fig. 16, and variance and flatness values are reported in Table 3. The variance is largest in the buffer layer across all flow cases, as expected because the near-wall peak of the fluid turbulent kinetic energy occurs in this region. In the buffer and log layers, the tails of the PDFs become slightly heavier as mass loading is increased. This may be due in part

Table 3
Variance (left) and flatness (right) of the particle velocity divergence normalised by the viscous time scale for different layers and mass loadings ϕ_0 with $St^+ = 7$.

ϕ_0	Viscous	Buffer	Log	ϕ_0	Viscous	Buffer	Log
0.1	6.06×10^{-3}	10.96×10^{-3}	2.15×10^{-3}	0.1	0.70×10^{2}	0.56×10^{2}	1.21×10^{2}
0.4	2.45×10^{-3}	12.12×10^{-3}	2.54×10^{-3}	0.4	7.21×10^{2}	1.15×10^{2}	3.91×10^{2}
1.0	1.79×10^{-3}	9.78×10^{-3}	2.47×10^{-3}	1.0	11.8×10^{2}	2.77×10^{2}	3.49×10^{2}

to the larger number of particles as ϕ_0 is increased, which offer more sampling to capture strong convergence/divergence, which occur less frequently, as described by Oujia et al. (2020), appendix A. This issue affects the viscous sublayer least, because turbophoresis makes the number density similar there, despite the overall change in mass loading. The variance of the divergence in the viscous sublayer decreases as ϕ_0 increases, which is likely due to the weaker velocity fluctuations as a result of two-way coupling. This would be expected from the theory of Esmaily and Mani (2020), who found that in general, the rate of expansion/contraction of particle clouds (i.e. their divergence) increases with the amplitude of the oscillations of the fluid flow. The greater variance for $\phi_0 = 0.1$ can be seen in Fig. 15(a) and 15(d), where a greater proportion of particles have zero divergence (green) at the higher mass loading. The changes to particle velocity divergence in the buffer and log layer due to mass loading are less substantial, probably due to stronger velocity fluctuations relative to the viscous sublayer, though there may be a weak maximum in variance at $\phi_0 = 0.4$, as shown in Table 3. The collision rate as a function of mass loading is shown in Fig. 17. As previously noted, the collision rate is highest in the buffer layer, as expected based on the variance of the particle velocity divergence. The collision rate decreases with mass loading across all flow regions, reflecting a general attenuation of turbulence as mass loading increases.

The values of flatness in Table 3 are much larger than 3, reflecting the strong intermittent behaviour in all cases and departure from Gaussianity. Moreover, the values increase with ϕ_0, except for the log-layer where the impact of ϕ_0 is much weaker.

Fig. 18 shows the three components of particle velocity curl across the flow regions. Like the previously shown PDFs of curl, C_z^+ is asymmetric with a negative mean, while C_x^+ and C_y^+ are nearly symmetric. Heavier tails as ϕ_0 is increased are again observed, possibly due to increased sampling at larger ϕ_0. A significant change due to mass loading is observed in the viscous sublayer, where the larger mass loading shows a narrower PDF with strongly decreased likelihood of $C_z^+ > 0$, i.e. locally reversed flow. Narrowing of the distribution is expected based on the tendency of particles to stabilise the near-wall streaks and attenuate velocity fluctuations. Similar to divergence, the particle velocity curl in x and y directions has the greatest variance in

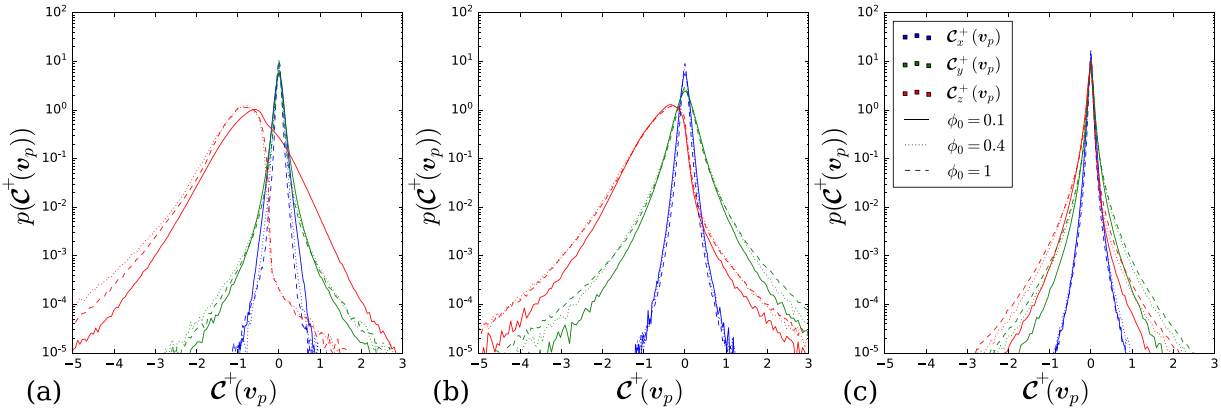

Fig. 18. PDF of three components of curl, normalised by the viscous time scale, for three different mass loadings with $St^+ = 7$, in the (a) viscous sublayer, (b) buffer layer, and (c) log layer. The line colour indicates the component of the curl, and the line style indicates the Stokes number.

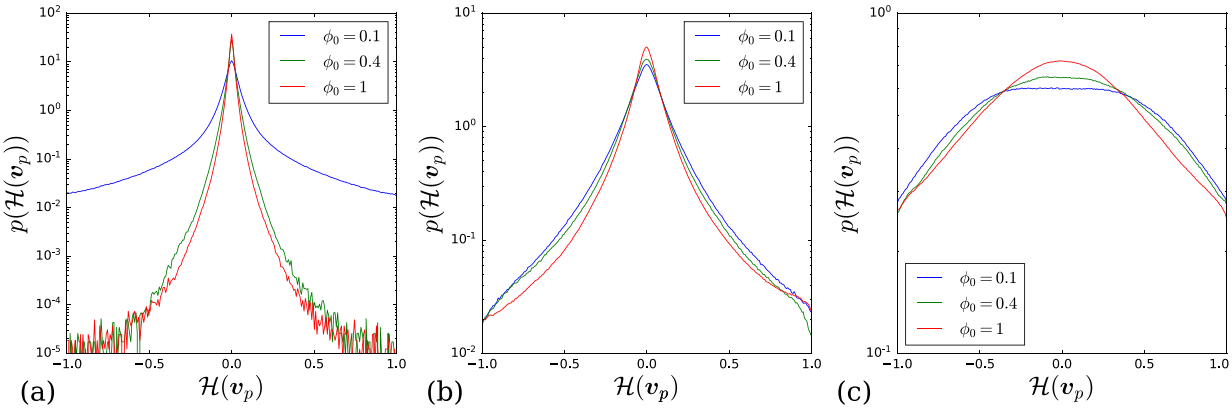

Fig. 19. PDFs of the relative helicity $\mathcal{H}(\boldsymbol{v}_p)$ of the particles for different mass loadings with $St^+ = 7$, in the (a) viscous sublayer, (b) buffer layer and (c) log layer. Note that the y-ranges differ by orders of magnitude.

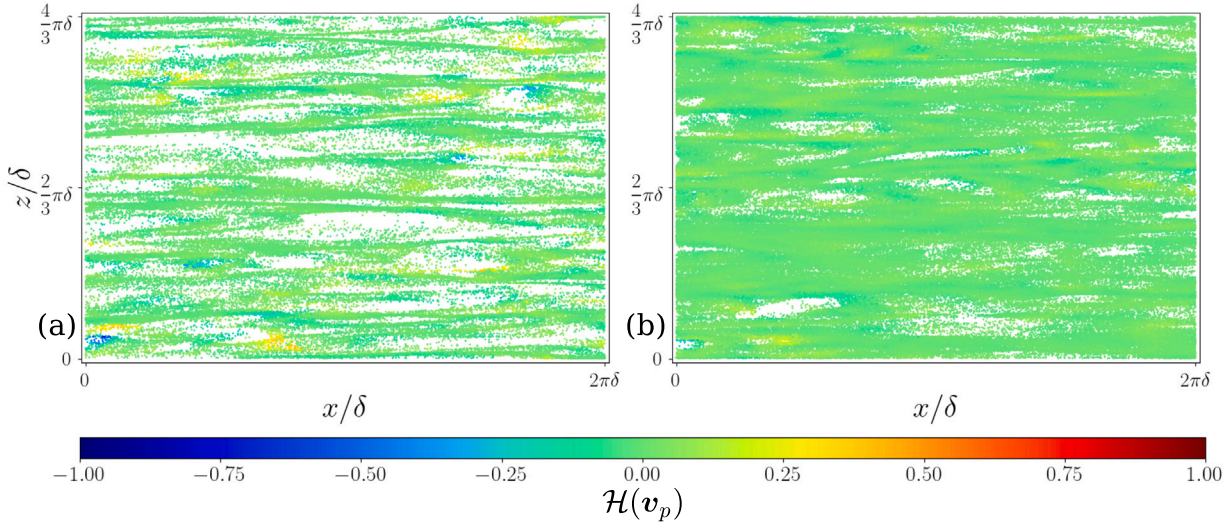

Fig. 20. Particle positions coloured by relative helicity in wall-parallel slices, for (a) viscous sublayer, $\phi_0 = 0.1$, $St^+ = 7$; (b) viscous sublayer, $\phi_0 = 0.4$, $St^+ = 7$.

the buffer layer, which suggests that active formation and annihilation of clusters is associated with stronger vortical motions. As in the fluid vorticity PDFs shown in Fig. 3, C_x^+ has a smaller variance than C_y^+ and C_z^+. Both fluid and particle vorticity show evidence of anisotropy due to two-way coupling. The fact that the curl is most isotropic in the log layer is also reflected in the particle visualisations in Fig. 15(c, f), which are qualitatively similar to previous results from HIT (Oujia et al., 2020).

Fig. 19 shows PDFs of the relative helicity of particle velocity for different mass loadings in the different layers. Much like the other

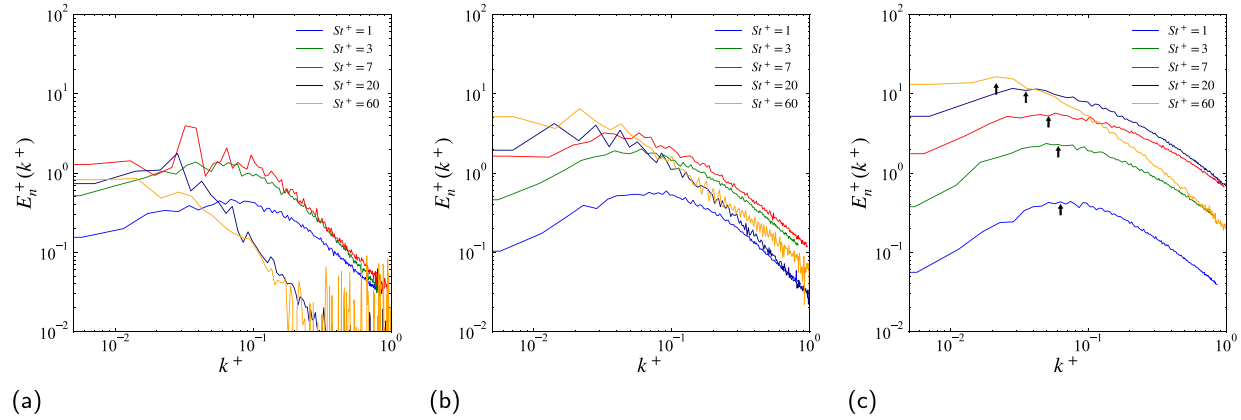

Fig. 21. Fourier spectra of particle number density in 2D slices in (a) viscous sublayer, (b) buffer, and (c) log layers for various Stokes numbers with $\phi_0 = 1$. The spectra and the wavenumber are normalised by the viscous length scale. In (c), the peak locations obtained with a five-point moving average are indicated with arrows.

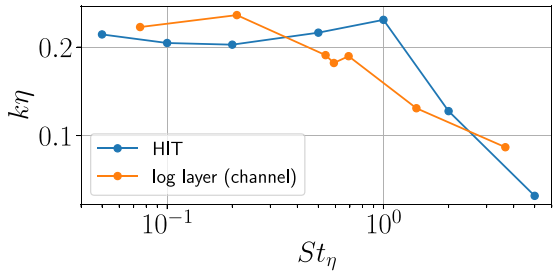

Fig. 22. Wavenumber of maximum in spectra of particle number density fluctuations as a function of Kolmogorov Stokes number for HIT (Matsuda et al., 2014) and the logarithmic layer in the present dataset.

results, the particle helicity is more likely to be zero the closer particles get to the wall. The effect of mass loading in the buffer layer and log layer is small, but in the viscous sublayer, the particle helicity distribution is significantly flatter with $\phi_0 = 0.1$. This indicates that the particle motion is more three-dimensional in this case. While it might be expected that this is due to a smaller degree of two-way coupling, this interpretation is not satisfying because the fluid helicity is much less, indicating that the particles are behaving somewhat independently of the fluid in this case. A similar observation was made about the large St^+ particles, and there is also a similarity in the PDF of C_z^+, which is significantly more symmetric at $\phi_0 = 0.1$ than large mass loadings. However, the particle distribution for $\phi_0 = 0.1$ is not random, but organised into streaky structures, suggesting a different cause than particles becoming ballistic and independent of the fluid, as happens at large St^+. This interpretation is confirmed by examining the visualisation of particles coloured by helicity in the viscous sublayer in Fig. 20. At $\phi_0 = 0.1$, the distribution of helicity is coherent, unlike the random speckles of helicity seen in Fig. 9(d) for $St^+ = 60$. The fact that Fig. 20(a, b) are both mostly green (zero helicity) underscores that particle swirling motion in the viscous sublayer is weak regardless of mass loading, and that the sharp apparent difference in PDFs in Fig. 19(a) is influenced by the logarithmic scale, and corresponds to slightly more intense, coherent helicity at $\phi_0 = 0.1$. A possible explanation is that the reduced two-way-coupling at small ϕ_0 allows for the transfer of more intensely swirling particle clusters from the buffer layer into the viscous sublayer. This is suggested by the fact that the helicity distribution in the viscous sublayer for ϕ_0 is quantitatively much closer to the distributions in the buffer layer than those in the viscous sublayer at other mass loadings.

Because the simulations used in this work are all four-way coupled, both the particle feedback force and collisions may play a role in explaining the trends observed as mass loading is increased. However, given that the largest volume fraction across the mass loading cases is $\alpha_0 = 1.35 \times 10^{-4}$, it is unlikely that collisions play significant role in the motion of particle clouds (Elghobashi, 1994). In addition, one-way coupled simulations would yield similar results to the lowest mass loading case ($\phi_0 = 0.1$), since the turbulence would not be affected by the presence of additional particles, and the Stokes number is constant across these simulations ($St^+ \approx 7$). Therefore, the trends observed as mass loading is varied should primarily be due to turbulence modulation from two-way coupling.

3.3. Fourier spectra of number density fluctuations

The preceding observations on divergence, curl, and helicity have shown how these quantities are attenuated or enhanced in different flow regions. However, in the PDFs presented, scale information has been lumped together. In this section, spectra of particle number density fluctuations are examined to ascertain which scales of clustering may contribute to the changes observed so far. As in the other sections, the domain is decomposed into wall-parallel slices to characterise the effect of flow region. The location and thickness of the slices are the same as the visualisation in Fig. 15, i.e. $2 \leq y^+ < 3$, $9.5 \leq y^+ < 14.5$ and $97.5 \leq y^+ < 102.5$ for viscous sublayer, buffer layer, and log layer, respectively. Each spectrum is averaged over the same 10 snapshots used to compute divergence, curl, and helicity.

The Fourier spectra of number density fluctuations for simulations at different St^+ are shown in Fig. 21. The spectra are normalised by the viscous length scale, i.e., $E_n^+(k^+) = E_n(k^+/l_{visc})/l_{visc}$ and $k^+ = kl_{visc}$. In the log layer, the Stokes number dependence is similar to that for HIT. Initially as St^+ is increased, the spectra shift vertically while the peak location remains at $k^+ \approx 0.08$, which corresponds to $k\eta \approx 0.2$ (η is the Kolmogorov scale), i.e. slightly smaller than Kolmogorov-scale eddies, which dominate clustering behaviour for small Stokes number. Then for sufficiently large Stokes number ($St^+ > 7$), the spectra move horizontally to smaller wavenumbers. The increased prevalence of large-scale clusters in the log layer for $St^+ = 60$ can be clearly seen by comparing the visualisations in Fig. 7(c, f). This shift is expected at $St_\eta = 1$ per Matsuda et al. (2014), and in the present data, it is observed around $St_\eta^{\log} \approx 0.5$. A comparison of peak location vs. Stokes number normalised by Kolmogorov scale is shown in Fig. 22 for both the present log layer data and the HIT data of Matsuda et al. (2014). Given the differences in Reynolds number, two-way coupling, and flow anisotropy, we find the quantitative similarity striking. As the peak location begins to shift significantly, the slope of the spectra at high wavenumbers in the log layer also becomes more negative in qualitative agreement with the results from Matsuda et al. (2014). This change in slope corresponds to the reduction in fine-scale clusters observed going from $St^+ = 3$ to $St^+ = 60$ in Fig. 7(c, f).

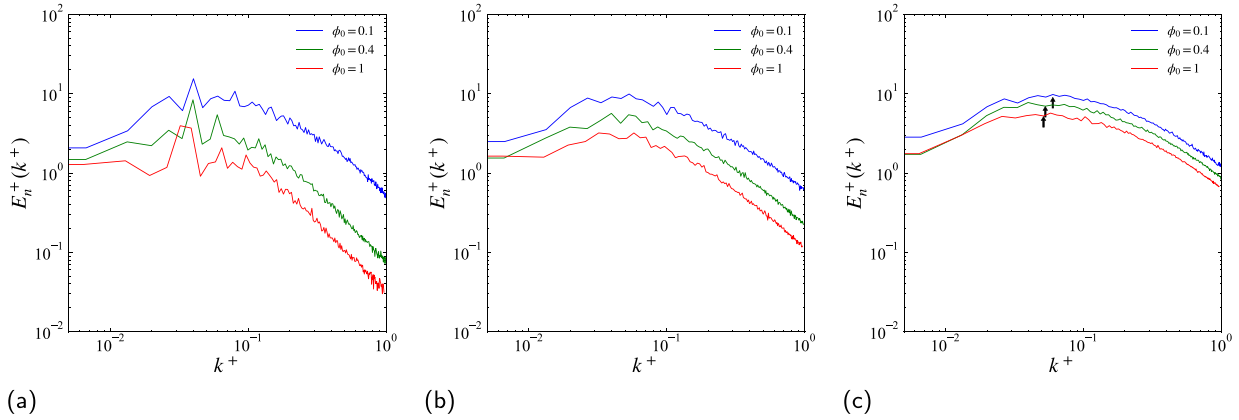

Fig. 23. Fourier spectra of particle number density on 2D slices in (a) viscous sublayer, (b) buffer, and (c) log layers for various mass loadings with $St^+ = 7$. The spectra and the wavenumber are normalised by the viscous length scale. In (c), the peak locations obtained with a five-point moving average are indicated with arrows.

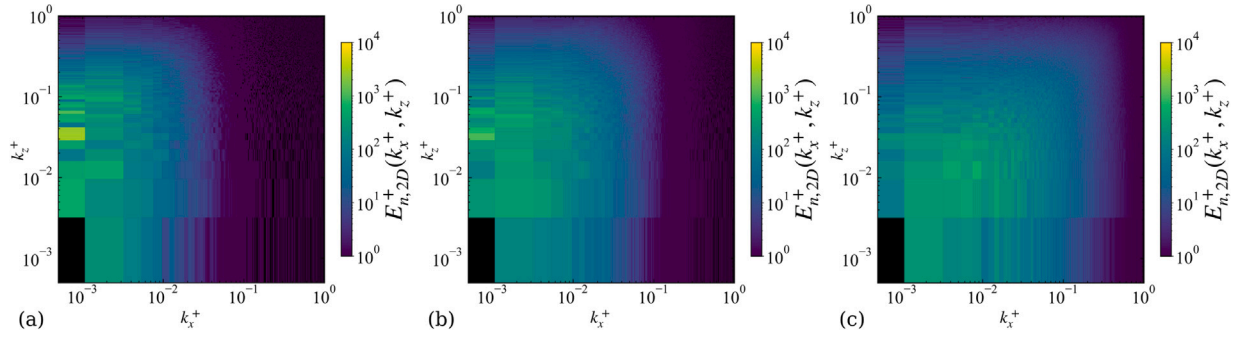

Fig. 24. 2D Fourier spectra of particle number density on 2D slices in (a) viscous sublayer, (b) buffer, and (c) log layers for $\phi_0 = 1.0$ and $St^+ = 7$. The spectra and the wavenumber are normalised by the viscous length scale. Areas appearing in black indicate regions where there is no particle distribution.

In the buffer layer, a similar horizontal shift to larger scales as St^+ is increased can also be observed, again corresponding to the increased prevalence of large-scale clusters and reduction in small-scale clusters seen in Fig. 21(b,c). In the viscous sublayer, the spectra are noisier, particularly at large St^+, because the particles become more randomly distributed, and the periodogram, used to estimate the spectrum, is an inconsistent estimator due to the presence of oscillations (Priestley, 1981).

Fig. 23 shows the spectra as a function of ϕ_0. In general, there is an attenuation at all scales across all layers as mass loading is increased. This is expected from the turbulence attenuation caused by two-way coupling (Fig. 2(c, d)). Similar to the PDFs of divergence, curl, and helicity, the attenuation in spectra is most dramatic in the viscous sublayer, except at the very largest scales (small wavenumbers). This suggests that the attenuation of clustering, vortical motion, and swirling as mass loading increases originate from small to moderate scales. The dominant scales in the viscous sublayer correspond to the length of and spacing between the low-speed streaks, which do not change drastically as ϕ_0 is increased from 0.1 to 1.0. In the buffer and log layers, the peak location does not shift much, which is expected because St^+ is approximately constant for the mass loading variation. This is confirmed by the visualisations in Fig. 15, which show similar scales of clustering, albeit with greater number density of particles, as ϕ_0 is increased.

Fig. 24 shows the 2D Fourier spectra of number density in k_x^+–k_z^+ plane for $\phi_0 = 1.0$ and $St^+ = 7$. Similar to Fig. 21, the spectra are normalised with viscous scales. In the log layer, the spectra is close to symmetry for the line of $k_x^+ = k_z^+$, meaning that the clustering is close to isotropic. However, in the viscous sublayer and buffer layer, the spectra is more significant in the k_z^+ direction (similar to the angular distribution functions in Fong et al., 2019), and the peak of the 2D spectra is located around $k_x^+ = 0$ and $k_z^+ = 3\times10^{-2}$. Thus, the spectra in Fig. 24(a, b) reflect the spanwise structure of clustering, especially the elongated chains of particles near the wall. Similar trends were found in the 2D spectra for the other ϕ_0 and St^+ cases.

4. Conclusions

In this study, tessellation-based methods for computing particle velocity divergence, curl, and helicity were applied to turbulent channel flow, and the influence of mass loading and Stokes number in various flow regions was examined in detail. Probability density functions (PDFs) of particle velocity divergence and curl reveal that these quantities vary most intensely in the buffer layer. Since turbulent kinetic energy peaks in the buffer layer, this implies that strong velocity fluctuations drive more intense cluster formation/destruction, as well as vorticity. In the viscous sublayer, particles form elongated clusters in the low-speed streaks, which are transported without converging or diverging. The wall boundary condition naturally results in a flow with less swirling motion than in the rest of the channel, and the presence of particles stabilises the viscous sublayer and makes the streaks longer-lived. This makes both the fluid and particle motions even more two-dimensional, except in the case of very large Stokes number.

In the logarithmic layer, many similarities with results for homogeneous isotropic turbulence (HIT) reported by Oujia et al. (2020, 2022) were observed. Particle clustering patterns, as well as distributions of divergence, curl, and helicity are qualitatively similar to one-way coupled particles in HIT, despite force coupling from the particle phase that increases the turbulence anisotropy in wall-bounded flows, and quantitative differences in Reynolds number. Furthermore, the spectra of particle number density fluctuations exhibit a similar dependence on Stokes number as compared to the HIT dataset of Matsuda et al. (2014).

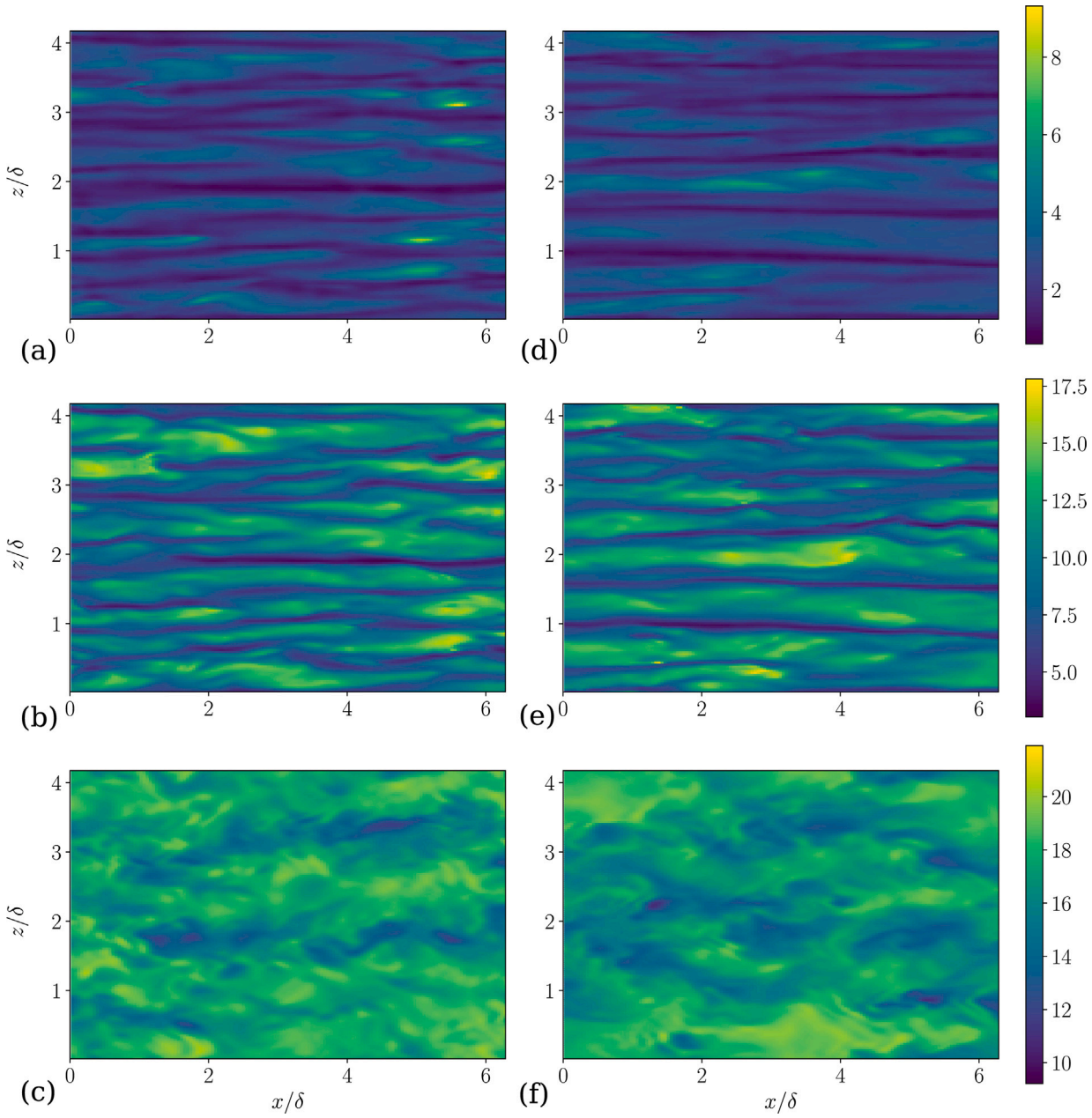

Fig. 25. Fluid streamwise velocity u^+ for (a) $\phi_0 = 0.1$, $St^+ = 7$ at $y^+ = 2.5$; (b) $\phi_0 = 0.1$, $St^+ = 7$ at $y^+ = 12$; (c) $\phi_0 = 0.1$, $St^+ = 7$ at $y^+ = 100$; (d) $\phi_0 = 0.4$, $St^+ = 7$ at $y^+ = 2.5$; (e) $\phi_0 = 0.4$, $St^+ = 7$ at $y^+ = 12$; (f) $\phi_0 = 0.4$, $St^+ = 7$ at $y^+ = 100$.

The dynamics of particle clusters in channel flow are affected similarly by Stokes number as they are in HIT, except in the viscous sublayer, where the relatively low turbulence intensity and proximity to wall boundary result in particles which behave more independently of the fluid. Like in HIT, increasing the Stokes number results in more intense convergence/divergence, as well as more intense rotational motion. This effect eventually saturates, except in the viscous sublayer, where particles become more independent of the relatively steady fluid flow. Due to the particle feedback force, both the fluid and particle motion become more two-dimensional (zero-helicity) in the log and buffer layers as Stokes number is increased. In the viscous sublayer, an initial attenuation is followed by an increase in swirling motion as St^+ is increased. This non-monotonic trend further illustrates the stark differences in clustering between the viscous sublayer and other flow regions.

The fact that similar trends are observed in the logarithmic layer and buffer layer in the present results as previous studies in one-way coupled HIT suggests that the principal driver of the observed trends is the same preferential concentration mechanism present in one-way coupled flows without particle feedback force or collisions. For a further quantitative argument about the causal effect of two-way coupling on the statistics, comparisons of the present four-way coupled simulations with one-way and two-way coupled simulations might be beneficial, particularly in the viscous sublayer, where different trends are observed with respect to Stokes number.

The effect of the mass loadings studied in this work is more subtle than the effect of Stokes number, but again, the viscous sublayer shows unique cluster dynamics. The changes observed in the viscous sublayer as mass loading is increased are that the variance of particle velocity divergence and curl are both decreased, and that swirling particle

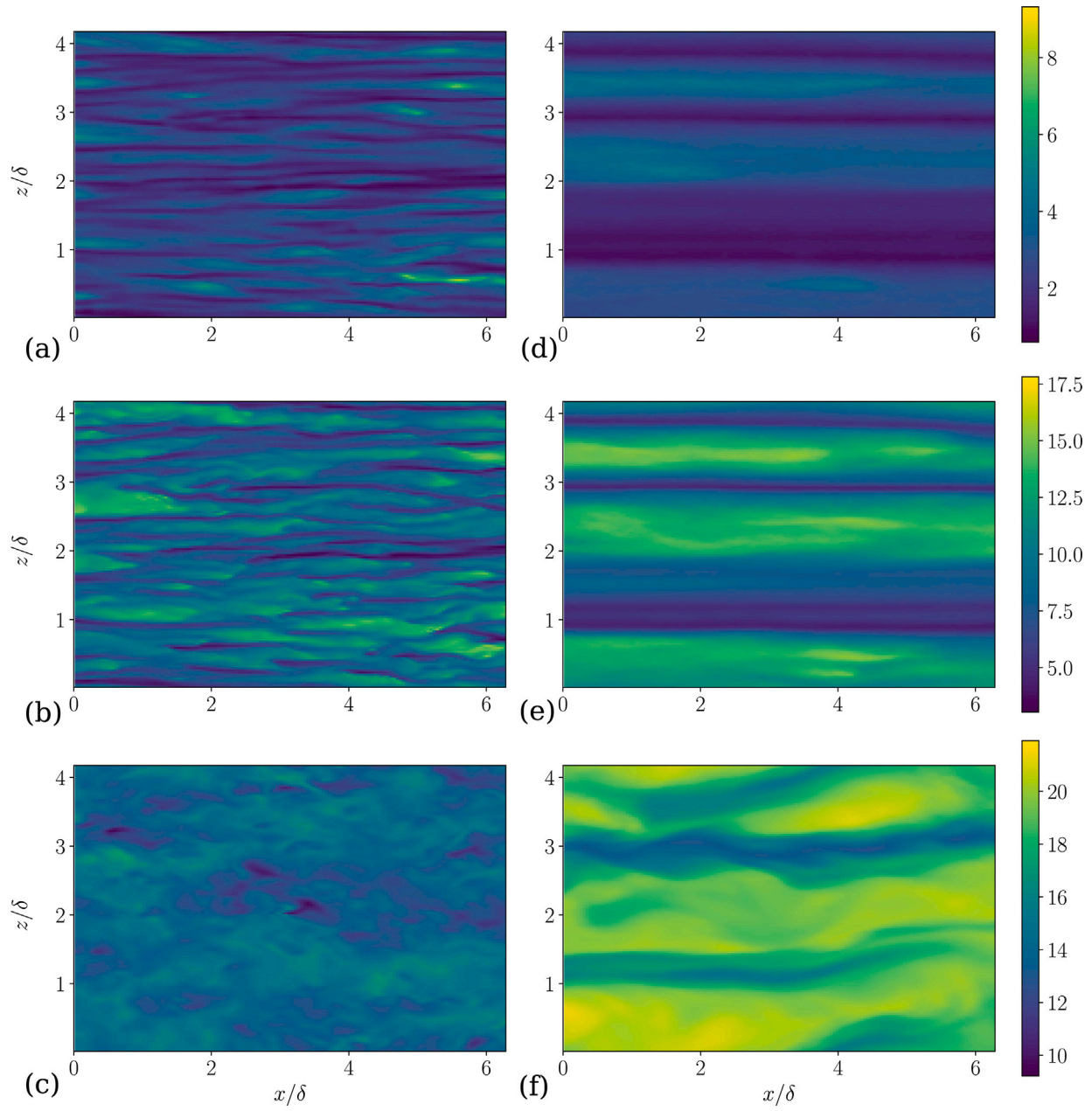

Fig. 26. Fluid streamwise velocity u^+ for (a) $\phi_0 = 1.0$, $St^+ = 3$ at $y^+ = 2.5$; (b) $\phi_0 = 1.0$, $St^+ = 3$ at $y^+ = 12$; (c) $\phi_0 = 1.0$, $St^+ = 3$ at $y^+ = 100$; (d) $\phi_0 = 1.0$, $St^+ = 60$ at $y^+ = 2.5$; (e) $\phi_0 = 1.0$, $St^+ = 60$ at $y^+ = 12$; (f) $\phi_0 = 1.0$, $St^+ = 60$ at $y^+ = 100$.

motions are attenuated. These changes are expected from turbulence attenuation due to particles, which results in more anisotropic turbulence and more persistent low-speed streaks near the wall. It is surprising that similar effects are not observed in the buffer and log layers, given that the inertia of fluid and particle phases are comparable at $\phi_0 = 1$, and the strong attenuation of the fluid-phase Reynolds stress that occurs over this range (Fig. 2(d)). Nevertheless, as mass loading increases from $\phi_0 = 0.1$ to $\phi_0 = 1.0$, there are only small changes to divergence, curl, and helicity in the buffer and log layers. Likewise, the spectra of number density fluctuations are much more strongly affected in the viscous sublayer as mass loading is increased than in other parts of the flow. The is consistent with the interpretation that in the logarithmic layer and buffer layer, one-way coupling effects, which are governed by Stokes number and not mass loading, are the main driver of particle clustering, rotation, and swirl for mass loadings up to $\phi_0 = 1$. Because the volume fractions are dilute, the changes in the motion of particle clouds observed as mass loading is varied are likely more due to turbulence attenuation from two-way coupling than collisions. We also acknowledge the possibility that further increasing the mass loading above $\phi_0 = 1$ would lead to greater changes in cluster dynamics throughout the flow because of further turbulence attenuation, and in this regime, additional one-way and two-way coupled simulations would be useful to differentiate the roles of collisions and the particle feedback force.

The PDFs based on particle motions not only quantify the cluster formation/annihilation, rotation, and swirling of particle clouds, but also are consistent with the structures seen in the visualisations, as well as the number density spectra. Thus, the present approach provides both statistical and structural insights into particle clustering in wall turbulence, which mean profiles and Eulerian analysis cannot do alone. The techniques used in this paper can also be applied to study clustering, rotation, and swirl of particle clouds in other regimes in the vast parameter space of particle-laden flows (Brandt and Coletti, 2022). For example, in flows with larger particle volume fraction, collisions

are expected to play a significant role, and their influence on the clustering, rotation, and swirling of particle clouds should be examined. In future work, wavelet-based statistics and multi-resolution analysis of particle clustering (Matsuda et al., 2022) can be used in conjunction with these techniques to better characterise the scale dependence of particle clustering, and how different scales of clusters contribute to the dynamics of particle clouds.

CRediT authorship contribution statement

Jacob R. West: Writing – original draft, Visualization, Software, Investigation, Formal analysis, Conceptualization. **Thibault Maurel–Oujia:** Writing – original draft, Visualization, Software, Investigation, Formal analysis, Conceptualization. **Keigo Matsuda:** Writing – original draft, Investigation, Formal analysis, Conceptualization. **Kai Schneider:** Writing – review & editing, Supervision, Investigation, Conceptualization. **Suhas S. Jain:** Writing – review & editing, Investigation, Conceptualization. **Kazuki Maeda:** Writing – review & editing, Supervision, Investigation, Conceptualization.

Declaration of competing interest

The authors declare that they have no known competing financial interests or personal relationships that could have appeared to influence the work reported in this paper.

Data availability

Data will be made available on request.

Acknowledgements

The authors acknowledge use of computational resources from the Yellowstone cluster awarded by the National Science Foundation to the Center for Turbulence Research (CTR).

Funding

This work was supported by the Center for Turbulence Research (CTR), United States during the 2022 Summer Program (T. Maurel–Oujia, K. Matsuda, K. Schneider), the Agence Nationale de la Recherche (ANR), France [grant number ANR-20-CE46-0010-01] (T. Maurel–Oujia, K. Schneider), the Japan Society for the Promotion of Science (JSPS) KAKENHI [grant number JP20K04298] (K. Matsuda), and the Advanced Simulation and Computing program of the US Department of Energy's National Nuclear Security Administration, United States via the PSAAP-II Center at Stanford [grant number DE-NA0002373] (J. R. West). S. S. Jain acknowledges funding from the Boeing Co. K. Maeda acknowledges funding from SRB Co., Ltd. and support from Purdue University, United States.

Appendix. Visualisations of fluid velocity

To gain a better sense of the changes in flow structure, instantaneous snapshots of streamwise velocity in the viscous sublayer, buffer layer and log layer are shown in Fig. 25, which compares mass loadings $\phi_0 = [0.1, 0.4]$, and Fig. 26, which compares Stokes numbers $St^+ = [3, 60]$ These show the same time snapshots as Figs. 7 and 15, respectively. The effect of increasing ϕ_0 from 0.1 to 0.4 is subtle, but in general results in an attenuation of smaller scales in the fluid velocity field. In the viscous sublayer and buffer layer, this manifests as more persistent and slightly more widely spaced near-wall streaks. The persistence and stability of streaky structures illustrates how particles stabilise the near-wall flow and dampen velocity fluctuations. The effect of changing St^+ from 3 to 60 is more extreme. Near-wall streaks become much more stable and wider at large St^+, and the streaks persist well into the log layer, which indicates that large St^+ particles can act to thicken the viscous sublayer, make the flow more two-dimensional, and eventually kill the turbulence. The thickening of the viscous sublayer at large St^+ can also be seen in the mean velocity profile in Fig. 2(a).

References

Andersson, H., Zhao, L., Variano, E., 2015. On the anisotropic vorticity in turbulent channel flows. J. Fluids Eng. 137, 084503.
Aurenhammer, F., 1991. Voronoi diagrams—a survey of a fundamental geometric data structure. ACM Comput. Surv. 23, 345–405.
Balachandar, S., Eaton, J., 2010. Turbulent dispersed multiphase flow. Annu. Rev. Fluid Mech. 42, 111–133.
Barber, C., Dobkin, D., Huhdanpaa, H., 1996. The quickhull algorithm for convex hulls. ACM Trans. Math. Software 22, 469–483.
Basu, P., 2006. Combustion and Gasification in Fluidized Beds. CRC Press.
Bose, S., 2012. Explicitly Filtered Large-Eddy Simulation: With Application to Grid Adaptation and Wall Modeling. Stanford University.
Bragg, A., Collins, L., 2014. New insights from comparing statistical theories for inertial particles in turbulence: I. Spatial distribution of particles. New J. Phys. 16, 055013.
Bragg, A., Richter, D., Wang, G., 2021. Settling strongly modifies particle concentrations in wall-bounded turbulent flows even when the settling parameter is asymptotically small. Phys. Rev. Fluids 6, 124301.
Brandt, L., Coletti, F., 2022. Particle-laden turbulence: Progress and perspectives. Annu. Rev. Fluid Mech. 54, 159–189.
Capecelatro, J., Desjardins, O., 2015. Mass loading effects on turbulence modulation by particle clustering in dilute and moderately dilute channel flows. J. Fluids Eng. 137, 111102.
Chen, L., Goto, S., Vassilicos, J., 2006. Turbulent clustering of stagnation points and inertial particles. J. Fluid Mech. 553, 143–154.
Coleman, S., Vassilicos, J., 2009. A unified sweep-stick mechanism to explain particle clustering in two- and three-dimensional homogeneous, isotropic turbulence. Phys. Fluids 21, 113301.
Costa, P., Brandt, L., Picano, F., 2021. Near-wall turbulence modulation by small inertial particles. J. Fluid Mech. 922, A9.
Dritselis, C., Vlachos, N., 2008. Numerical study of educed coherent structures in the near-wall region of a particle-laden channel flow. Phys. Fluids 20, 055103.
Elghobashi, S., 1994. On predicting particle-laden turbulent flows. Appl. Sci. Res. 52, 309–329.
Esmaily, M., Horwitz, J., 2018. A correction scheme for two-way coupled point-particle simulations on anisotropic grids. J. Comput. Phys. 375, 960–982.
Esmaily, M., Mani, A., 2020. Modal analysis of the behavior of inertial particles in turbulence subjected to Stokes drag. Phys. Rev. Fluids 5, 084303.
Esmaily, M., Villafane, L., Banko, A., Iaccarino, G., Eaton, J., Mani, A., 2020. A benchmark for particle-laden turbulent duct flow: A joint computational and experimental study. Int. J. Multiph. Flow 132, 103410.
Esmaily-Moghadam, M., Mani, A., 2016. Analysis of the clustering of inertial particles in turbulent flows. Phys. Rev. Fluids 1, 084202.
Farge, M., Pellegrino, G., Schneider, K., 2001. Coherent vortex extraction in 3D turbulent flows using orthogonal wavelets. Phys. Rev. Lett. 87 (5), 054501.
Fessler, J., Kulick, J., Eaton, J., 1994. Preferential concentration of heavy particles in a turbulent channel flow. Phys. Fluids 6, 3742–3749.
Février, P., Simonin, O., Squires, K., 2005. Partitioning of particle velocities in gas–solid turbulent flows into a continuous field and a spatially uncorrelated random distribution: Theoretical formalism and numerical study. J. Fluid Mech. 533, 1–46.
Fong, K., Amili, O., Coletti, F., 2019. Velocity and spatial distribution of inertial particles in a turbulent channel flow. J. Fluid Mech. 872, 367–406.
Frankel, A., Iaccarino, G., Mani, A., 2017. Optical depth in particle-laden turbulent flows. J. Quant. Spectrosc. Radiat. Transfer 201, 10–16.
Ho, C., 2016. A review of high-temperature particle receivers for concentrating solar power. Appl. Therm. Eng. 109, 958–969.
Hutter, K., 2005. Geophysical granular and particle-laden flows: Review of the field. Philos. Trans. R. Soc. A 363, 1497–1505.
Kuerten, J.G.M., 2016. Point-particle DNS and LES of particle-laden turbulent flow-a state-of-the-art review. Flow Turbul. Combust. 97, 689–713.
Kuerten, J., Vreman, A., 2016. Collision frequency and radial distribution function in particle-laden turbulent channel flow. Int. J. Multiph. Flow 87, 66–79.
Kulick, J., Fessler, J., Eaton, J., 1994. Particle response and turbulence modification in fully developed channel flow. J. Fluid Mech. 277, 109–134.
Lee, J., Lee, C., 2015. Modification of particle-laden near-wall turbulence: Effect of Stokes number. Phys. Fluids 27, 023303.
Lee, J., Lee, C., 2019. The effect of wall-normal gravity on particle-laden near-wall turbulence. J. Fluid Mech. 873, 475–507.
Li, Y., McLaughlin, J., Kontomaris, K., Portela, L., 2001. Numerical simulation of particle-laden turbulent channel flow. Phys. Fluids 13, 2957–2967.
Liu, Y., Shen, L., Zamansky, R., Coletti, F., 2020. Life and death of inertial particle clusters in turbulence. J. Fluid Mech. 902, R1.

Marchioli, C., Soldati, A., 2002. Mechanisms for particle transfer and segregation in a turbulent boundary layer. J. Fluid Mech. 468, 283–315.
Matsuda, K., Onishi, R., Hirahara, M., Kurose, R., Takahashi, K., Komori, S., 2014. Influence of microscale turbulent droplet clustering on radar cloud observations. J. Atmos. Sci. 71, 3569–3582.
Matsuda, K., Onishi, R., Kurose, R., Komori, S., 2012. Turbulence effect on cloud radiation. Phys. Rev. Lett. 108, 224502.
Matsuda, K., Schneider, K., Oujia, T., West, J., Jain, S., Maeda, K., 2022. Multiresolution analysis of inertial particle tessellations for clustering dynamics. In: Proceedings of the Summer Program. Center for Turbulence Research, Stanford University.
Maurel-Oujia, T., Matsuda, K., Schneider, K., 2023. Computing differential operators of the particle velocity in moving particle clouds using tessellations. J. Comput. Phys. 2023, 112658.
Maxey, M., 1987. The gravitational settling of aerosol particles in homogeneous turbulence and random flow fields. J. Fluid Mech. 174, 441–465.
Moffatt, H.K., Tsinober, A., 1992. Helicity in laminar and turbulent flow. Annu. Rev. Fluid Mech. 24 (1), 281–312.
Monchaux, R., Bourgoin, M., Cartellier, A., 2010. Preferential concentration of heavy particles: A Voronoï analysis. Phys. Fluids 22, 103304.
Nilsen, C., Andersson, H., Zhao, L., 2013. A Voronoï analysis of preferential concentration in a vertical channel flow. Phys. Fluids 25, 115108.
Oujia, T., Matsuda, K., Schneider, K., 2020. Divergence and convergence of inertial particles in high-Reynolds-number turbulence. J. Fluid Mech. 905 (A14).
Oujia, T., Matsuda, K., Schneider, K., 2022. Extreme divergence and rotation values of the inertial particle velocity in high Reynolds number turbulence using delaunay tessellation. In: 12th International Symposium on Turbulence and Shear Flow Phenomena. TSFP12, Osaka, Japan, p. 2022.
Priestley, M., 1981. Spectral Analysis and Time Series, Academic.
Reeks, M., 1983. The transport of discrete particles in inhomogeneous turbulence. J. Aerosol Sci. 14, 729–739.
Richter, D., Sullivan, P., 2013. Momentum transfer in a turbulent, particle-laden couette flow. Phys. Fluids 25, 053304.
Robinson, S., 1991. Coherent motions in the turbulent boundary layer. Annu. Rev. Fluid Mech. 23, 601–639.
Rogers, M., Moin, P., 1987. Helicity fluctuations in incompressible turbulent flows. Phys. Fluids 30, 2662–2671.
Sardina, G., Schlatter, P., Brandt, L., Picano, F., Casciola, C., 2012. Wall accumulation and spatial localization in particle-laden wall flows. J. Fluid Mech. 699, 50–78.
Schiller, L., Naumann, Z., 1935. A drag coefficient correlation. Zeit. Ver. Deutsch Ing. 77, 318–320.
Soldati, A., Marchioli, C., 2009. Physics and modelling of turbulent particle deposition and entrainment: Review of a systematic study. Int. J. Multiph. Flow 35, 827–839.
Squires, K., Eaton, J., 1991. Preferential concentration of particles by turbulence. Phys. Fluids A 3, 1169–1178.
Vance, M., Squires, K., Simonin, O., 2006. Properties of the particle velocity field in gas-solid turbulent channel flow. Phys. Fluids 18, 063302.
Vreman, A., 2007. Turbulence characteristics of particle-laden pipe flow. J. Fluid Mech. 584, 235–279.
Wang, L., Wexler, A., Zhou, Y., 2000. Statistical mechanical description and modelling of turbulent collision of inertial particles. J. Fluid Mech. 415, 117–153.
West, J.R., 2023. Flow Physics of Radiatively Heated Particle-Laden Channel Flow and Simulation Methods for Shock-Driven Problems in Materials with Strength. Stanford University.
West, J.R., Oujia, T., Matsuda, K., Schneider, K., Jain, S.S., Maeda, K., 2022. Divergence and curl of the inertial particle velocity in a four-way coupled turbulent channel flow. In: Proceedings of the Summer Program. Center for Turbulence Research, Stanford University.
Zhao, L., Andersson, H., Gillissen, J., 2013. Interphasial energy transfer and particle dissipation in particle-laden wall turbulence. J. Fluid Mech. 715, 32–59.